Available online at www.sciencedirect.com
ScienceDirect
Comput. Methods Appl. Mech. Engrg. 373 (2021) 113474
Computer methods in applied mechanics and engineering
www.elsevier.com/locate/cma

A combined finite element–finite volume framework for phase-field fracture

Juan Michael Sargado[a,b,*], Eirik Keilegavlen[a], Inga Berre[a], Jan Martin Nordbotten[a]

[a] *Department of Mathematics, University of Bergen, Allégaten 41, 5007 Bergen, Norway*
[b] *NORCE Norwegian Research Centre AS, Nygårdsporten, Bergen, Norway*

Received 2 May 2019; received in revised form 4 September 2020; accepted 24 September 2020
Available online 21 October 2020

Abstract

Numerical simulations of brittle fracture using phase-field approaches often employ a discrete approximation framework that applies the same order of interpolation for the displacement and phase-field variables. In particular, the use of linear finite elements to discretize both stress equilibrium and phase-field equations is widespread in the literature. However, the use of P_1 Lagrange shape functions to model the phase-field is not optimal, as the latter contains cusps for fully developed cracks. These should in turn occur at locations corresponding to Gauss points of the associated FE model for the mechanics. Such a feature is challenging to reproduce accurately with low order elements, and element sizes must consequently be made very small relative to the phase-field regularization parameter in order to achieve convergence of results with respect to the mesh. In this paper, we combine a standard linear FE discretization of stress equilibrium with a cell-centered finite volume approximation of the phase-field evolution equation based on the two-point flux approximation constructed over the same simplex mesh. Compared to a pure FE formulation utilizing linear elements, the proposed framework results in looser restrictions on mesh refinement with respect to the phase-field length scale. This ability to employ coarser meshes relative to the traditional implementation allows for significant reductions on computational cost, as demonstrated in several numerical examples.

Keywords: Fracture; Phase-field models; Finite element; Finite volume

1. Introduction

Brittle fracture is an important failure mechanism against which engineering structures must be properly designed to ensure their safety. At the same time, the deliberate initiation and propagation of fractures are central to many subsurface applications related to energy production and waste disposal. Griffith [1] was the first to formulate a theory of brittle fracture based on thermodynamic arguments, utilizing earlier results by Inglis [2] concerning stresses around elliptical holes. This theory was later amended to include the effect of plastic zones around crack tips by Irwin, who also introduced the notion of stress intensity factors [3]. Together, these form the basis of classical linear elastic fracture mechanics (LEFM). More recently, an extension to LEFM in the form of a variational theory of

* Correspondence to: Danish Hydrocarbon Research and Technology Centre, Technical University of Denmark, Denmark.
E-mail addresses: jmiuy@dtu.dk (J.M. Sargado), Eirik.Keilegavlen@uib.no (E. Keilegavlen), Inga.Berre@uib.no (I. Berre), Jan.Nordbotten@uib.no (J.M. Nordbotten).

https://doi.org/10.1016/j.cma.2020.113474

fracture was formulated by Francfort and Marigo [4], with the aim of overcoming the former's limitations regarding crack initiation and branching through the adoption of an energy minimization framework.

Establishment of the finite element method in the early 1960s also fueled the development of numerical techniques for simulating fracture in solid structures, and nowadays the work of Ngo and Scordelis [5] and Rashid [6] on crack formation in concrete are recognized as pioneering efforts in discrete and continuous approaches to fracture modeling. In the former, cracks are treated as discrete/sharp entities, and the introduction of new crack segments can be realized explicitly via inter-element separation algorithms [7,8], ideally in combination with adaptive remeshing in order to remove mesh bias. As brittle material behavior is characterized by the occurrence of stress singularities at crack tips, this necessitates considerable mesh refinement in order to accurately resolve local stress fields. A classical way of dealing with this problem is to make use of quarter-point elements [9]. Alternatively, an implicit treatment of discrete cracks can be made through enrichment of the approximation space by suitable functions that directly model displacement discontinuities and stress singularities, as in the extended finite element method [10,11]. With smeared crack approaches on the other hand, no effort is made to track the fracture surfaces. Instead, material stiffness is progressively reduced in order to approximate the overall mechanical response arising from the presence of a crack. Notable developments in this category include the fictitious crack model [12], rotating smeared cracks [13], the crack band model [14], integral-type damage theory [15], implicit gradient-enhanced damage models [16,17], and variational phase-field models [18,19]. The last in particular have been gaining massive popularity in recent years due to their clear connection to Griffith's theory. In these models, cracks are represented as diffuse entities through an auxiliary scalar variable ϕ known as the phase-field [20], with the amount of diffusion being controlled by a regularization parameter ℓ. While the initial intent of [18] was for the regularized energy functional to approximate a body with discrete cracks through the concept of Γ-convergence [21], lately it has come to be understood that variational phase-field models are in fact a subset of gradient-enhanced damage models, and that the phase-field regularization parameter should be related to the intrinsic length scale of the material [22–25].

The main strength of the phase-field method relative to other approaches is the ease with which complex evolution of fractures can be modeled. In particular, its underlying energy minimization framework automatically handles the branching of fractures without the need to introduce external criteria. Furthermore since cracks are modeled by a single field, no additional complexity involving bookkeeping of surface intersections and the like is introduced upon the initiation and branching/coalescence of cracks. Instead, an additional partial differential equation must be solved that governs the auxiliary field evolution. This makes the approach promising for multiphysics applications where the interaction between different physical processes due to fracture formation can be recast in a diffuse setting, essentially becoming a coupling term that is additionally dependent on the phase-field. Such applications have included thermal cracking [24,26], electro-mechanical processes [27,28], fluid-driven fracture in elastic and poroelastic materials [29–34], and chemo-mechanical degradation of battery electrode particles [35,36]. On the other hand, a prevailing challenge in the use of fracture phase-field models is the computational expense associated with their solution, primarily due to the nonlinear coupling of the component PDEs and also the need to properly resolve the diffuse cracks in the mesh according to the phase-field length scale. While the crack tip stress singularities associated with discrete approaches are eliminated in the phase-field formulation [23], selective mesh refinement is nevertheless required since the phase-field profile for fully developed cracks contains cusps as illustrated in Fig. 1. Consequently, the discretization must be suitably fine in the vicinity of cracks to resolve rapidly changing gradients. This can in turn dramatically increase the computational size of the discrete problem, particularly if the crack path is unknown a priori and a global mesh refinement strategy is used. As an alternative, one can make use of adaptive local refinement strategies in order to achieve the required element sizes in the vicinity of crack paths. This has been explored in several works, for instance [37–42]. In some of these works, both the element size h and the phase-field length scale ℓ are simultaneously reduced following the concept of Γ-convergence, with ℓ expressed as a function of h or vice versa. While such a strategy may be applied in cases where fracture propagation proceeds from a preexisting crack, it is important to note that for crack nucleation in the absence of stress singularities, the relevant parameter is the material strength which in turn has a dependence on both the critical energy release rate $\mathcal{G}_c$ and ℓ [25]. In this case, ℓ must be kept at a fixed value while h is refined in order to properly capture the irregularity of the phase-field profile. An interesting idea introduced in [43] is that of anisotropic mesh adaptation. This capitalizes on the fact that meshes need to be refined mainly along the direction of steep phase-field gradients, which can be accomplished by using elements with high aspect ratios.

Another important consideration in the phase-field approach is the non-convexity of the regularized functional used to approximate the Griffith energy. Imposing stationarity of this functional yields two nonlinear coupled

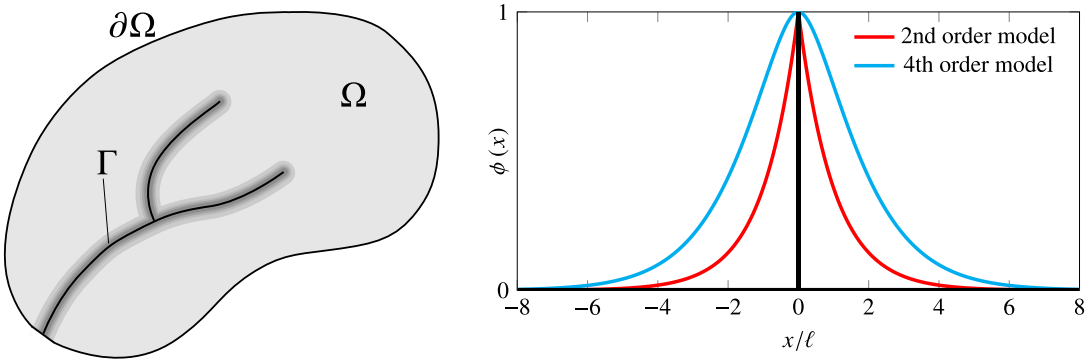

(a) (b)

Fig. 1. Phase-field modeling of fractures. (a) Discrete cracks Γ are assumed to be surfaces of dimension $n-1$ embedded inside an n-dimensional body; these are represented as diffuse entities via an auxiliary scalar field $\phi \in [0, 1]$. (b) Phase-field profile for a 1-dimensional body with a fully developed crack at $x = 0$. The classical 2nd order phase-field model results in ϕ having a cusp at the crack location, which can be rounded by using a higher order model as proposed for instance in [44].

PDEs representing stress equilibrium and incremental energy balance, and it is well known that straightforward application of the Newton–Raphson method to solve the resulting discrete system leads to divergence of iterations when cracks are growing. Use of the alternate minimization (AM) algorithm to solve the aforementioned system was first proposed in [18], and this remains the method of choice in many subsequent works due to its robustness. However the AM algorithm achieves only linear convergence, and a large amount of iterations is often needed in order to achieve convergence during crack growth. A one-pass staggered scheme was introduced in [45], which eliminates the issue of having to perform iterations at the cost of requiring sufficiently small time steps in order to achieve acceptable accuracy. It was later demonstrated in [46] that this scheme is inadequate for use in conjunction with arc-length approaches, even when time steps are kept extremely small. A special line search algorithm was developed in [47] for use with a fully monolithic approach, with the aim of recovering convergence by finding for each iteration the solution that yields the global minimum of the energy along a given search direction. In particular, it was shown that the energy functional may vary in a very complex manner along a given direction, and that a very accurate reconstruction of this variation is required in order to find the true minimum needed to restore convergence of the monolithic scheme. On the other hand, the idea of constructing a convex approximation of the regularized energy is explored in [40]. This is accomplished by performing a linear extrapolation of the phase-field using values from previous time steps for use in the stress equilibrium equation. The algorithm can be interpreted as an extension of the one-pass staggered scheme, with the latter using phase-field values from the previous time step directly in lieu of an extrapolation. Augmentation of the standard AM scheme by over-relaxation was also investigated in [48], where it was combined with a backtracking line search-assisted Newton scheme to reduce the number of overall iterations needed for convergence.

With regard to the discrete function spaces used to numerically approximate the coupled system of PDEs, the standard practice thus far has been to employ the same order of basis functions for the linear momentum and phase-field equations. In addition, while earlier studies utilizing FEM such as [20,49] favored setting the characteristic size of elements to half the magnitude of ℓ in conjunction with P_1 basis functions, this ratio has been found to be suboptimal in later studies [50,51]. Higher order models have also been introduced which result in looser requirements on the mesh resolutions with respect to ℓ due to blunting of the cusp, however such models require C^1-continuous solutions for the phase-field and hence are more suited for use with specialized schemes that preserve higher order continuity, such as isogeometric basis functions [44] and local maximum entropy approximants [52]. An interesting direction recently explored in [53] combines discrete approaches (in the form of extended finite elements) with the phase-field method, in which the latter is restricted to local domains surrounding crack tips in order to limit the overall size of the discrete problem.

In this contribution, we propose a combined discretization scheme (in the sense of both unequal-order approximation and different formulations) to solve the coupled system of equations associated with phase-field modeling of brittle fracture. The idea is based on the assumption that the need to properly resolve the phase-field along

cracks leads to mesh size restrictions that are more stringent than what is needed for the accurate resolution of the regularized stresses. Within a finite element context, this naturally leads to the prospect of using higher order basis functions for the auxiliary field. Alternatively, one can make use of an approximation scheme that can better handle the lack of regularity associated with phase-field solutions for fully developed cracks. In particular for this paper, we look at the prospect of adopting control volume formulation approaches such as finite volumes. Compared with methods based on a weak formulation such as FEM, the use of finite volumes in solid mechanics applications has not been as extensively explored, and to our knowledge the earliest application thus far of the latter in phase-field fracture can be found in [54], where an FV discretization is utilized for all of the governing equations. In this work, we propose instead to combine a finite element approximation of the linear momentum equation using P_1 shape functions with a cell-centered finite volume scheme for the phase-field subsystem based on the classical two-point flux approximation (TPFA). The phase-field is assumed to be piecewise constant over elements, hence our scheme is effectively a P_1-P_0 formulation. However, the main advantage of a finite volume scheme in this case is that it allows for discontinuous gradients within a local cell while preserving the continuity of normal derivative terms across cell faces. This in turn is ideal for modeling the cusps that occur in the phase-field profile. Furthermore, local calculations pertaining to a cell do not involve matrix operations and hence are much cheaper to carry out than those associated with a variational formulation such as finite elements. A limitation of the TPFA is that it ignores the tangential components of gradients across cell faces. Hence in porous media flow applications for which the technique was originally developed, the cell faces should be aligned with the principal directions of the permeability tensor in order to produce correct results [55]. On the other hand in the PDE governing fracture evolution, the relevant material parameter acting on the phase-field gradient is the critical energy release rate, $\mathcal{G}_c$. For a wide class of materials, $\mathcal{G}_c$ is specified as a scalar quantity that can alternatively be interpreted as an isotropic tensor, and our experience in this case has been that application of TPFA to unstructured simplex meshes yields acceptable results despite cell faces being generally non-orthogonal.

2. Mathematical formulation

Let us consider a solid body occupying a domain Ω and containing a collection of internal cracks denoted by Γ. Following [4], we assume that its total potential energy may be expressed as a sum of bulk and surface terms. That is,

$$\Psi = \int_{\Omega\setminus\Gamma} \psi_0\left(\boldsymbol{\varepsilon}\right)\, \mathrm{d}\Omega + \int_{\Gamma} \mathcal{G}_c\, \mathrm{d}\Gamma, \tag{1}$$

wherein $\psi_0\left(\boldsymbol{\varepsilon}\right) = \frac{1}{2}\lambda\left(\operatorname{tr}\boldsymbol{\varepsilon}\right)^2 + \mu\boldsymbol{\varepsilon} : \boldsymbol{\varepsilon}$ is the Helmholtz free energy for the bulk material, and $\mathcal{G}_c$ is the critical energy release rate from Griffith's theory of brittle fracture [1]. As the second term represents the energy dissipation associated with crack formation, it is further subject to the irreversibility constraint

$$\Gamma\left(t + \Delta t\right) \supseteq \Gamma\left(t\right) \tag{2}$$

for $\Delta t > 0$, meaning that cracks may only grow over time but not heal. Determining the proper evolution of Γ under arbitrary loading conditions is nontrivial, and following [19] we instead utilize a regularized version of the above potential, expressed as

$$\Psi_\ell = \int_{\Omega} \psi\left(\boldsymbol{\varepsilon}, \phi\right)\, \mathrm{d}\Omega + \int_{\Omega} \mathcal{G}_c \gamma_\ell\left(\phi, \nabla\phi\right)\, \mathrm{d}\Omega. \tag{3}$$

In the above expression, the cracks have been recast as diffuse entities, with $\gamma_\ell\left(\phi, \nabla\phi\right)$ representing the crack surface density per unit volume, or analogously the crack length per unit area for 2-dimensional problems. In particular we adopt a form derived in [49] and given by

$$\gamma_\ell\left(\phi, \nabla\phi\right) = \frac{1}{2\ell}\phi^2 + \frac{\ell}{2}\nabla\phi \cdot \nabla\phi. \tag{4}$$

The scalar variable $\phi \in [0, 1]$ is known as the crack phase-field, and characterizes respectively for $\phi = 0$ and $\phi = 1$ the fully pristine and fully broken states of a material. On the other hand, ℓ is a regularization parameter (the phase-field length scale) that controls the amount of diffusion in the crack representation.

There are several ways to regularize the bulk term in (1). In the present study, we make use of two different regularizations: the isotropic model

$$\psi\left(\boldsymbol{\varepsilon},\phi\right)=g\left(\phi\right)\psi_0\left(\boldsymbol{\varepsilon}\right) \tag{5}$$

originally employed in [18], and an anisotropic model for approximating unilateral contact developed by Amor et al. [56], given by

$$\begin{aligned}\psi\left(\boldsymbol{\varepsilon},\phi\right)&=g\left(\phi\right)\left[\frac{\kappa}{2}\left(\mathrm{tr}^{+}\,\boldsymbol{\varepsilon}\right)^2+\mu\boldsymbol{\varepsilon}_{\mathrm{dev}}:\boldsymbol{\varepsilon}_{\mathrm{dev}}\right]+\frac{\kappa}{2}\left(\mathrm{tr}^{-}\,\boldsymbol{\varepsilon}\right)^2\\&=g\left(\phi\right)\psi_0^{+}\left(\boldsymbol{\varepsilon}\right)+\psi_0^{-}\left(\boldsymbol{\varepsilon}\right),\end{aligned} \tag{6}$$

in which $\boldsymbol{\varepsilon}_{\mathrm{dev}}$ denotes the deviatoric component of $\boldsymbol{\varepsilon}$ (see Appendix), and $\mathrm{tr}^{\pm}\,\boldsymbol{\varepsilon}$ is defined as

$$\begin{aligned}\mathrm{tr}^{+}\,\boldsymbol{\varepsilon}&=\max\left(0,\mathrm{tr}\,\boldsymbol{\varepsilon}\right)\\\mathrm{tr}^{-}\,\boldsymbol{\varepsilon}&=\min\left(0,\mathrm{tr}\,\boldsymbol{\varepsilon}\right).\end{aligned} \tag{7}$$

Both models above involve an energy degradation function $g\left(\phi\right)$, whose role is to annihilate material stiffness at locations where the material is broken according to the phase-field. For simplicity, we adopt the quadratic expression

$$g\left(\phi\right)=\left(1-\phi\right)^2 \tag{8}$$

that is most often used in the literature. Nevertheless we note that the above form is not the most optimal for use with (4), and in particular for accurate modeling of failure loads as well as overall linear response prior to fracture we refer the reader to our previous work on parametric degradation functions [51].

To obtain the governing equations for the brittle fracture problem, we first define a functional that includes both the potential energy and external work terms, i.e.

$$\Pi=\Psi_\ell-\int_\Omega\mathbf{b}\cdot\mathbf{u}\,\mathrm{d}\Omega-\int_{\partial\Omega^N}\mathbf{t}\cdot\mathbf{u}\,\mathrm{d}\partial\Omega \tag{9}$$

in which $\mathbf{b}$ denotes the body force, and $\mathbf{t}$ the surface traction acting on the Neumann boundary $\partial\Omega^N$. Imposing stationarity of the above functional, we have

$$\delta\Pi=0=\frac{\partial\Pi}{\partial\mathbf{u}}\delta\mathbf{u}+\frac{\partial\Pi}{\partial\phi}\delta\phi \tag{10}$$

which yields two coupled PDEs corresponding to the different terms on the right hand side above. The first term is none other than the weak form of the stress equilibrium equation:

$$\int_\Omega\boldsymbol{\sigma}\left(\boldsymbol{\varepsilon},\phi\right):\delta\boldsymbol{\varepsilon}\,\mathrm{d}\Omega=\int_\Omega\mathbf{b}\cdot\delta\mathbf{u}\,\mathrm{d}\Omega+\int_{\partial\Omega^N}\mathbf{t}\cdot\delta\mathbf{u}\,\mathrm{d}\partial\Omega, \tag{11}$$

wherein $\boldsymbol{\sigma}\left(\boldsymbol{\varepsilon},\phi\right)=\partial\psi\left(\boldsymbol{\varepsilon},\phi\right)/\partial\boldsymbol{\varepsilon}$. On the other hand, expanding the second term in (10) yields the weak form of the phase-field evolution equation, given by

$$\int_\Omega\mathcal{G}_c\left(\frac{1}{\ell}\phi\,\delta\phi+\ell\nabla\phi\cdot\nabla\delta\phi\right)\mathrm{d}\Omega+\int_\Omega g'\left(\phi\right)\psi_0^{+}\left(\boldsymbol{\varepsilon}\right)\,\mathrm{d}\Omega=0. \tag{12}$$

As in [18], we impose homogeneous natural conditions on the entire external boundary, i.e.

$$\nabla\phi\cdot\mathbf{n}=0\quad\text{on }\partial\Omega, \tag{13}$$

where $\mathbf{n}$ is the outward unit normal vector to $\partial\Omega$. Performing integration by parts and imposing arbitrariness of $\delta\mathbf{u}$ and $\delta\phi$, we obtain the strong form of coupled system given by the following boundary value problem:

$$\begin{cases}\nabla\cdot\boldsymbol{\sigma}\left(\boldsymbol{\varepsilon},\phi\right)+\mathbf{b}=\mathbf{0} & \text{in }\Omega & \text{(14a)}\\\mathbf{u}=\bar{\mathbf{u}} & \text{on }\partial\Omega^D & \text{(14b)}\\\boldsymbol{\sigma}\left(\boldsymbol{\varepsilon},\phi\right)\cdot\mathbf{n}=\mathbf{t} & \text{on }\partial\Omega^N & \text{(14c)}\\\mathcal{G}_c\ell\nabla^2\phi-\dfrac{\mathcal{G}_c}{\ell}\phi=g'\left(\phi\right)\psi_0^{+}\left(\boldsymbol{\varepsilon},\phi\right) & \text{in }\Omega & \text{(14d)}\\\nabla\phi\cdot\mathbf{n}=0 & \text{on }\partial\Omega. & \text{(14e)}\end{cases}$$

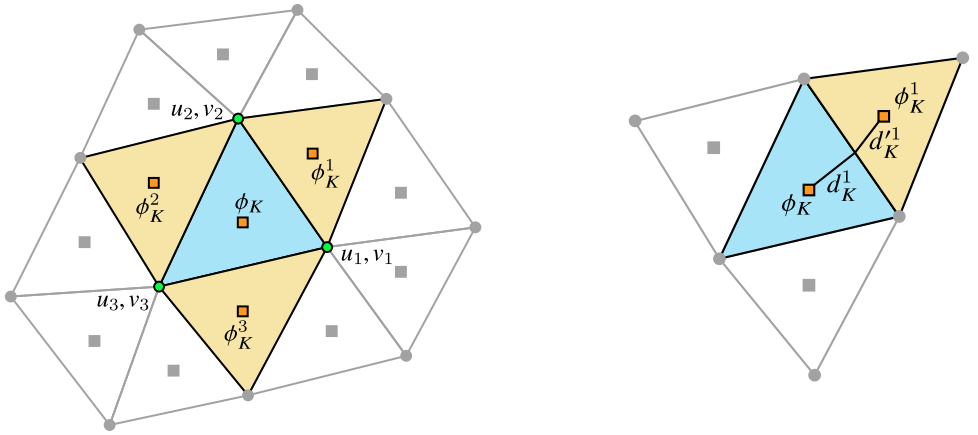

Fig. 2. Discrete formulation of the phase-field brittle fracture problem, combining P_1 finite elements for the linear momentum equation and cell-centered finite volumes for the phase-field evolution equation. (a) Computational stencil for Ω_K, and (b) distances from respective cell centers to the face midpoint that are used to calculate the transmissibility coefficient M_K^1 between Ω_K and Ω_K^1.

It then remains to enforce the irreversibility of crack growth. Here we adopt the approach of Miehe et al. [45] and replace ψ_0^+ with a history field defined as

$$\mathcal{H}(\mathbf{x}, t) = \begin{cases} \max_{s\in[0,t]} \psi_0^+ (\boldsymbol{\varepsilon}(\mathbf{x}, s)), & \phi > \phi_c \\ \psi_0^+ (\boldsymbol{\varepsilon}(\mathbf{x}, t)) & \text{otherwise.} \end{cases} \tag{15}$$

in which ϕ_c is some chosen irreversibility threshold.

3. Computational framework

3.1. Discrete approximation

To perform a numerical solution of the coupled system, we combine a finite element formulation of the linear momentum equation using P_1 basis functions with a cell-centered finite volume discretization of the phase-field equation based on the two-point flux approximation. Fig. 2(a) shows the resulting computational stencil for an interior triangular cell Ω_K, which involves displacement degrees of freedom at the cell vertices and phase-field DOFs located at cell centers of Ω_K and its immediate surrounding cells, denoted by Ω_K^i. To construct the local matrices pertaining to a given cell, we begin by expressing the displacement and strain fields in Voigt form as vector quantities, i.e. $\mathbf{u} = \{u_x, u_y\}^{\mathrm{T}}$ and $\boldsymbol{\varepsilon} = \{\varepsilon_{xx}, \varepsilon_{yy}, \varepsilon_{zz}, \gamma_{xy}\}^{\mathrm{T}}$. These are then interpolated over a given element as

$$\begin{aligned} \mathbf{u} &= \sum_{I=1}^{3} \mathbf{N}_I \mathbf{u}_I \qquad \delta\mathbf{u} = \sum_{I=1}^{3} \mathbf{N}_I \delta\mathbf{u}_I \\ \boldsymbol{\varepsilon} &= \sum_{I=1}^{3} \mathbf{B}_I \mathbf{u}_I \qquad \delta\boldsymbol{\varepsilon} = \sum_{I=1}^{3} \mathbf{B}_I \delta\mathbf{u}_I, \end{aligned} \tag{16}$$

in which the matrices $\mathbf{N}_I$ and $\mathbf{B}_I$ are given by

$$\mathbf{N}_I = \begin{bmatrix} N_I & 0 \\ 0 & N_I \end{bmatrix} \qquad \mathbf{B}_I = \begin{bmatrix} N_{I,x} & 0 \\ 0 & N_{I,y} \\ 0 & 0 \\ N_{I,y} & N_{I,x} \end{bmatrix} \tag{17}$$

corresponding to plane strain conditions. N_I and $\mathbf{u}_I$ are respectively the standard Lagrange (P_1) shape function and displacement vector associated with node I, and $N_{I,x}$ and $N_{I,y}$ are the derivatives of N_I with respect to x and y. Let

us consider a local element Ω_K having area A_K. The damaged-reduced stress $\boldsymbol{\sigma}(\boldsymbol{\varepsilon}, \phi)$ is assumed to be constant over Ω_K, hence the local residual for the discretized linear momentum equation associated with node I can be integrated using one Gauss point located at the center of Ω_K. This yields

$$\mathbf{r}_I^{\mathbf{u}} = A_K \mathbf{B}_I^{\mathrm{T}} \boldsymbol{\sigma}(\boldsymbol{\varepsilon}, \phi) - A_K \mathbf{N}_I^{\mathrm{T}} \mathbf{b} - \int_{\left(\partial\Omega_{\mathbf{u}}^N\right)_K} \mathbf{N}_I^{\mathrm{T}} \mathbf{t}\, \mathrm{d}S. \tag{18}$$

Meanwhile, we construct the discrete approximation of the residual pertaining to the phase-field equation by first integrating (14d) over Ω_K and applying integration by parts to obtain the corresponding control volume formulation:

$$\begin{aligned} 0 &= \int_{\Omega_K} \left(g'(\phi)\, \mathcal{H} + \frac{\mathcal{G}_c}{\ell}\phi - \mathcal{G}_c \ell \nabla^2 \phi \right) \mathrm{d}\Omega \\ &= \int_{\Omega_K} \left[g'(\phi)\, \mathcal{H} + \frac{\mathcal{G}_c}{\ell}\phi - \nabla \cdot (\mathcal{G}_c \ell \nabla \phi) \right] \mathrm{d}\Omega \\ &= \int_{\Omega_K} \left[g'(\phi)\, \mathcal{H} + \frac{\mathcal{G}_c}{\ell}\phi_K \right] \mathrm{d}\Omega - \int_{\partial\Omega_K} \mathcal{G}_c \ell \nabla \phi \cdot \mathbf{n}\, \mathrm{d}\partial\Omega_K \end{aligned} \tag{19}$$

Assuming ϕ to be piecewise constant over Ω_k, the residual for the phase-field equation can be written as

$$r_K^{\phi} = A_K \left[g'(\phi_K)\, \mathcal{H}_K + \frac{\mathcal{G}_{cK}}{\ell_K}\phi_K \right] + \sum_{i=1}^{3} M_K^i \left(\phi_K - \phi_K^i \right) \tag{20}$$

wherein A_K is the cell area, ϕ_K the value of phase-field inside Ω_K, and $\mathcal{G}_{cK}$ and ℓ_K are respectively the values of the critical energy release rate and phase-field regularization parameter within Ω_K. Meanwhile ϕ_K^i denotes the phase-field value at the adjacent cell sharing edge i with cell K, and M_K^i is the transmissibility coefficient associated with the edge $\partial\Omega_K^i$, defined as

$$M_K^i = \frac{L_i}{\dfrac{d_K^i}{\mathcal{G}_{cK}\ell_K} + \dfrac{d_k'^i}{\mathcal{G}_{cK}^i \ell_K^i}} \tag{21}$$

in which L_i is the length of edge i, and d_K^i and $d_K'^i$ are the respective distances from the centers of Ω_K and Ω_K^i to the midpoint of $\partial\Omega_K^i$ as illustrated in Fig. 2(b). We note that (20) is valid only when Ω_K is an interior cell. For cells situated at the boundary, one must account for prescribed boundary conditions acting on cell edges.

3.2. Nonlinear solution

The system unknowns $\{\mathbf{u}_I\}$ and $\{\phi_K\}$ are obtained by enforcing the condition

$$\begin{cases} \mathbf{r}_I^{\mathbf{u}} = \mathbf{0} & \text{(a)} \\ r_K^{\phi} = 0 & \text{(b)} \end{cases} \tag{22}$$

for each node I and cell K of the discretized domain. Due to the forms of $\boldsymbol{\sigma}(\boldsymbol{\varepsilon}, \phi)$ and $g(\phi)$, the global system is nonlinear and must be solved iteratively. Linearization of the local system yields

$$\begin{bmatrix} \mathbf{K}^u & \mathbf{K}^{u\phi} \\ \mathbf{K}^{\phi u} & \mathbf{K}^{\phi} \end{bmatrix} \begin{Bmatrix} \dot{\mathbf{u}} \\ \dot{\boldsymbol{\phi}} \end{Bmatrix} = \begin{Bmatrix} \mathbf{r}^u \\ r^{\phi} \end{Bmatrix} \tag{23}$$

in terms of the corrections $\dot{\mathbf{u}}$ and $\dot{\boldsymbol{\phi}}$, wherein

$$\mathbf{K}_{IJ}^u = A_K \mathbf{B}_I^{\mathrm{T}} \mathbb{C}(\boldsymbol{\varepsilon}, \phi)\, \mathbf{B}_J \tag{24}$$

$$\mathbf{K}_I^{u\phi} = A_K \mathbf{B}_I^{\mathrm{T}} \frac{\partial \boldsymbol{\sigma}(\boldsymbol{\varepsilon}, \phi)}{\partial \phi} \tag{25}$$

$$\mathbf{K}_J^{\phi u} = \mathbf{K}_I^{u\phi\,\mathrm{T}} \tag{26}$$

$$\mathbf{K}^{\phi} = \begin{bmatrix} A_K \left(g''(\phi_k)\, \mathcal{H}_K + \dfrac{\mathcal{G}_{cK}}{\ell_K} \right) + \sum_{i=1}^{3} M_K^i, & -M_K^1, & -M_K^2, & -M_K^3 \end{bmatrix} \tag{27}$$

	u_1	v_1	u_2	v_2	u_3	v_3	ϕ_K	ϕ_K^1	ϕ_K^2	ϕ_K^3
u_1	K_{11}^u	K_{12}^u	K_{13}^u	K_{14}^u	K_{15}^u	K_{16}^u	$K_1^{u\phi}$	0	0	0
u_2	K_{21}^u	K_{22}^u	K_{23}^u	K_{24}^u	K_{25}^u	K_{26}^u	$K_2^{u\phi}$	0	0	0
u_3	K_{31}^u	K_{32}^u	K_{33}^u	K_{34}^u	K_{35}^u	K_{36}^u	$K_3^{u\phi}$	0	0	0
u_4	K_{41}^u	K_{42}^u	K_{43}^u	K_{44}^u	K_{45}^u	K_{46}^u	$K_4^{u\phi}$	0	0	0
u_5	K_{51}^u	K_{52}^u	K_{53}^u	K_{54}^u	K_{55}^u	K_{56}^u	$K_5^{u\phi}$	0	0	0
u_6	K_{61}^u	K_{62}^u	K_{63}^u	K_{64}^u	K_{65}^u	K_{66}^u	$K_6^{u\phi}$	0	0	0
ϕ_K	$K_1^{\phi u}$	$K_2^{\phi u}$	$K_3^{\phi u}$	$K_4^{\phi u}$	$K_5^{\phi u}$	$K_6^{\phi u}$	K_1^{ϕ}	K_2^{ϕ}	K_3^{ϕ}	K_4^{ϕ}

Fig. 3. Local coefficient matrix profile for the proposed FE–FV scheme.

Note that while the resulting global set of equations involves a symmetric coefficient matrix, the local system given by (23) is not square as illustrated in Fig. 3. In order to deal with the non-convexity of (9) with respect to the pair of arguments $(\mathbf{u}, \phi)$, we make use of the alternate minimization algorithm introduced in [18] that is known to be robust for these types of problems. In each iteration of the AM algorithm, we first solve for the displacement unknowns with the phase-field fixed. Said displacements are then updated, after which the proper values of the history field are computed and the phase-field subsystem solved (with displacements fixed) and updated. This is carried out repeatedly until the corrections to $\mathbf{u}$ and ϕ as well as the residuals for each subsystem are within specified tolerances.

3.3. Initialization of phase-field for initial cracks

Many problems of interest feature preexisting cracks in the domain. These can be either built in to the initial geometry, or modeled via the phase-field which must then be initialized to account for the preexisting cracks. The latter can be accomplished in different ways. Some works such as [38,41] have advocated for initialization of the history field with the use of ad hoc procedures. These essentially involve performing global searches and nearest-distance calculations, and furthermore do not elaborate on how to treat locations in the immediate vicinity of multiple intersecting cracks.

A simpler alternative is to impose $\phi = 1$ as a Dirichlet constraint at the location of initial cracks throughout the entire duration of the simulation. For the FE–FV scheme employed in the present work, the phase-field unknowns lie at the cell centers so that the aforementioned constraint can be trivially applied if the domain is discretized such that initial cracks pass through element centers. On the other hand in a finite element scheme where phase-field unknowns are located at nodes, one can instead construct the mesh such that initial cracks align with element edges. However this runs into the problem of crack thickening when the domain is subjected to loading, a phenomenon that we demonstrate later in the numerical examples. A better procedure would be to adopt the same strategy as for the FV scheme (i.e. construct the mesh such that initial cracks pass through element centers), and then impose $\phi = 1$ on all nodes of elements that contain crack segments.

3.4. Implementation aspects

Both the proposed FE–FV formulation in the current work as well as the traditional discrete formulation utilizing equal-order P_1 FE basis functions are implemented within the software framework BROOMStyx [57], a general multiphysics simulator that allows for the combination of different discretization schemes with minimal overhead. Furthermore, the implementations for both formulations are optimized by storing quantities such as gradient matrices that do not vary with time at each evaluation point. Note that the incurred memory footprint of this is larger for the FE formulation in the phase-field subsystem, since it requires storage of both a 2-by-3 gradient matrix and a 3-by-3 mass matrix. In contrast, the FV scheme only needs to store transmissibility coefficients which amount to a single scalar value per local cell edge. The code is designed to run in parallel on shared memory architectures by means of

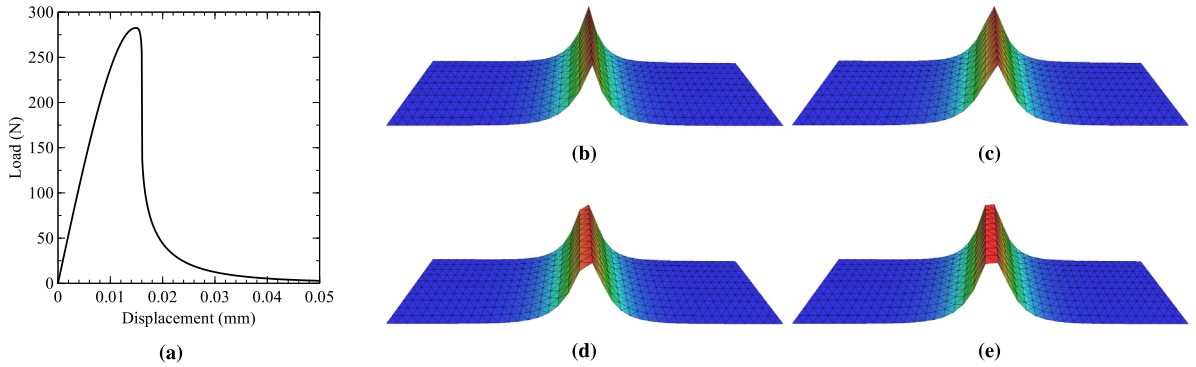

Fig. 4. Spurious growth of initialized phase-field for rectangular specimen under tensile loading, showing (a) the development of residual load as the imposed displacement is increased. The remaining figures show the phase-field profile at (b) $u_x = 0$, (c) $u_x = 0.058$, (d) $u_x = 0.017$, and (e) $u_x = 0.05$.

OpenMP directives, and dense matrix operations are carried out using BLAS and LAPACK routines provided by the Intel Math Kernel Library (MKL). Likewise, shared memory-parallel solution of sparse linear systems is performed using the direct solver PARDISO that is included in MKL. We do not perform adaptive remeshing during the course of our simulations, hence the initial sparsity profiles of global coefficient matrix do not change. As in [51], we exploit this property to speed up the solution of linear systems, specifically by performing symbolic factorization only at the beginning iteration of a substep, and thereafter proceeding directly to the numerical factorization phase of the solver in subsequent iterations. Additionally since both formulations result in symmetric global coefficient matrices, only the upper triangular portion of said matrices are actually assembled and manipulated by the linear solver which cuts down further the time for each iteration.

4. Numerical examples

In this section, we compare performance of the proposed FE–FV formulation against linear finite element approximation of both the linear momentum and phase-field equations. All 2-dimensional problems are solved assuming plane strain behavior, and the corresponding simulations are run in parallel on a desktop machine equipped with a single Intel i7-8700K (6-core) processor at 3.70 GHz base frequency. Each simulation run uses all 12 hyper-threads during execution of parallel regions such as the assembly of global coefficient matrices and right hand sides, and also during solution of sparse linear systems. Finally, all 2D meshes were generated using the software Gmsh [58].

4.1. Stretching of specimen fully cut by a crack

To demonstrate how the use of cell-centered finite volumes to discretize the phase-field equation improves over linear finite elements, we begin with a basic example involving a rectangular specimen occupying the domain $\Omega = [-10, 10] \times [0, 5]$ (dimensions in mm) and fully cut by a crack at $\{0\} \times [0, 5]$. The material parameters are set to $E = 210$ GPa, $\nu = 0.3$ and $\mathcal{G}_c = 2.7$ N/mm. For simplicity, we set $\ell = 1$ mm. The specimen is discretized using a symmetric configuration of uniform structured simplex elements having characteristic length $h = \ell/2$. Here we utilize linear FE approximations of both the mechanics and phase-field equations, and in particular the crack is modeled by imposing the Dirichlet condition $\phi = 1$ along the specimen centerline. Furthermore, we have constructed the mesh to use an even number of elements along the specimen length so that the crack location coincides with a row of element edges. In this way, the characteristic kink of the phase-field profile is handled naturally by the piecewise-continuous nature of the FE shape functions.

After initializing the phase-field, we impose a horizontal displacement $u_x = 0.05$ mm that is applied in 500 uniform increments on the boundary $\{10\} \times [0, 5]$, with additional constraints $u_x = 0$ on $\{-10\} \times [0, 5]$ and $u_y = 0$ on $[-10, 10] \times \{0\}$. In a continuous setting, no internal load should be induced by this stretching since the specimen

is already fully cracked. However for the discrete problem, one can observe a residual internal load that grows with increasing displacement towards a peak value before dropping again to zero as shown in Fig. 4(a). This can be explained by the fact that since $\phi = 1$ is imposed over a row of element edges, the values of ϕ at relevant element Gauss points are actually less than 1. This leads to some residual stiffness as then $g(\phi) > 0$ at these points. In addition, the residual bulk energy associated with the induced loads also induces further growth of the phase-field. Initially this is seen to occur symmetrically about the line where $\phi = 1$. However at some point bifurcation-type behavior is observed to occur such that $\phi = 1$ is achieved over a single row of elements (as opposed to two adjacent rows, which are energetically unfavorable). This is illustrated in Figs. 4(b)–4(e), where the final configuration can be understood as the actual 'stable' profile of the phase-field under tensile loading.

Based on the above results, we can simplify our initial comparison of FE and FV schemes by considering the 1-D problem of an infinitely long uniform cylindrical bar that is completely cut by a crack at $x = 0$. The bar is unstressed, and we are concerned only with solving for the phase-field profile. Hence the relevant governing equation is given by

$$\ell\phi''(x) - \frac{1}{\ell}\phi(x) = 0 \quad \forall x \in (-\infty, \infty), \tag{28}$$

subject to the boundary condition $\phi'(\pm\infty) = 0$ together with the internal condition $\phi(0) = 1$. As with the previous problem, we set $\ell = 1$. The analytical solution is then given by

$$\phi(x) = \exp(-|x|). \tag{29}$$

For convenience, we perform numerical solution over the truncated domain $-10 < x < 10$ with the understanding that $\phi'(\pm 10)$ is sufficiently close to zero so as to justify comparison with the above analytical solution. In a general discrete setting where the mechanics and phase-field equations are fully coupled, evolution of ϕ is driven by the source term $g'(\phi)\,\psi^+(\boldsymbol{\varepsilon})$ so that the phase-field should achieve its maximum values at the discrete locations where the source term is applied. In a finite element approximation of the mechanics, stresses and strains are naturally defined at element Gauss points, which are then the natural choice of locations for application of the phase-field source term. In the case of P_1 FE, said Gauss points coincide with element midpoints. In order to achieve the same effect in the decoupled phase-field equation, the domain is discretized such that the coordinate $x = 0$ is located at the center of an element. In the FV simulation, the effect of a source term acting on this central element is mimicked by setting the value of its associated DOF to unity. On the other hand for the FE setup, the constraint $\phi = 1$ is applied at the nodes of the same element. Fig. 5 shows the results of both methods for a domain partitioned into 21 uniformly sized cells of size $h = 0.952$. We can observe that although the phase-field is assumed to be constant within each cell for the FV solution, the value of ϕ at the center of each cell is much closer to the analytical solution compared to that obtained using finite elements. This can be attributed to the fact that approximation of the gradient terms at element endpoints by means of two-point fluxes effectively treats ϕ as discontinuous inside each cell, thus accommodating the presence of a cusp at $x = 0$.

We also study the effect of mesh refinement on the accuracy of both methods by means of the L_2-norm of the error, defined as

$$\|\phi - \phi_h\|_{L_2} = \sqrt{\int_\Omega (\phi - \phi_h)^2 \, \mathrm{d}\Omega} \tag{30}$$

Results are plotted in Fig. 6, where $h \in \left\{\frac{20}{11}, \frac{20}{21}, \frac{20}{41}, \frac{20}{81}, \frac{20}{161}, \frac{20}{321}, \frac{20}{641}\right\}$. We can see that while the error converges at the same rate in the L_2-norm for both methods, the accuracy obtained with finite volumes is better, being about the same as that for a finite element solution using a mesh with element sizes reduced by two. Cell-centered finite volumes are thus a cost-effective alternative to P_1 FE for the phase-field sub-problem, and in particular the factor two is found to hold also for higher dimensions as demonstrated in the succeeding examples.

4.2. Tension test of notched specimen

The tensile (mode-I) fracturing of a notched square specimen is a benchmark problem originally introduced by Miehe et al. [49] for demonstrating the capability of the phase-field approach to model brutal cracking. The specimen geometry and boundary conditions along with details of the a priori mesh refinement are shown in Fig. 7,

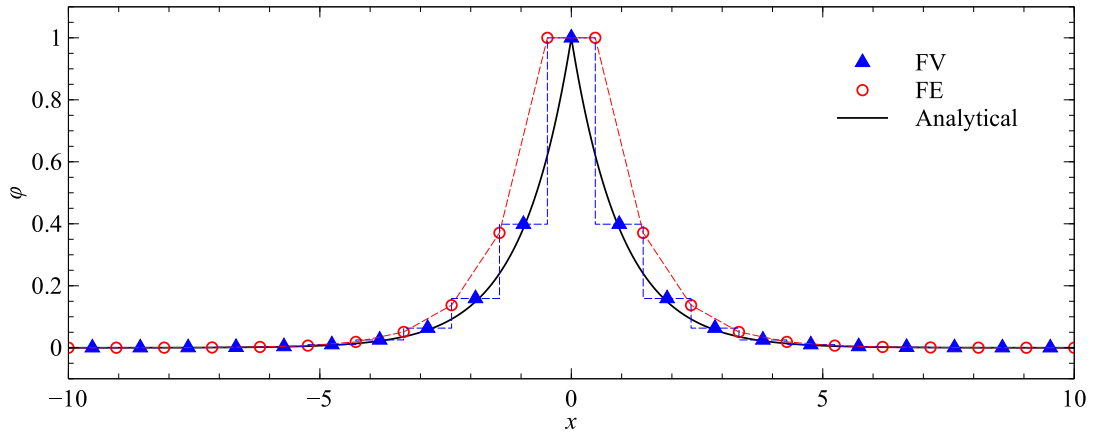

Fig. 5. Numerical solutions for the phase-field corresponding to a fully developed crack at $x = 0$ obtained using cell-centered FVM (TPFA) versus FEM (P_1). Dashed lines show how ϕ is interpolated locally within each element.

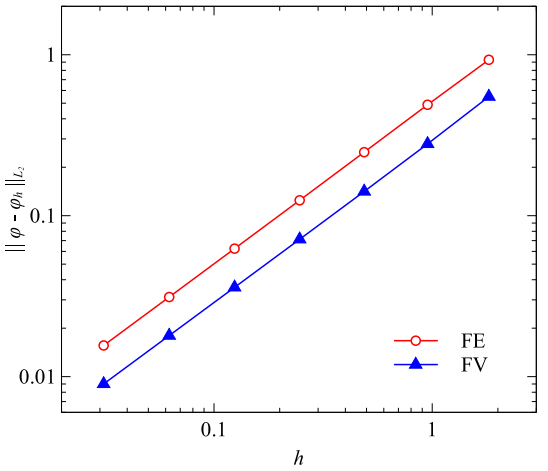

Fig. 6. Convergence of FE and FV solutions of the phase-field profile with respect to mesh refinement for the 1-dimensional problem.

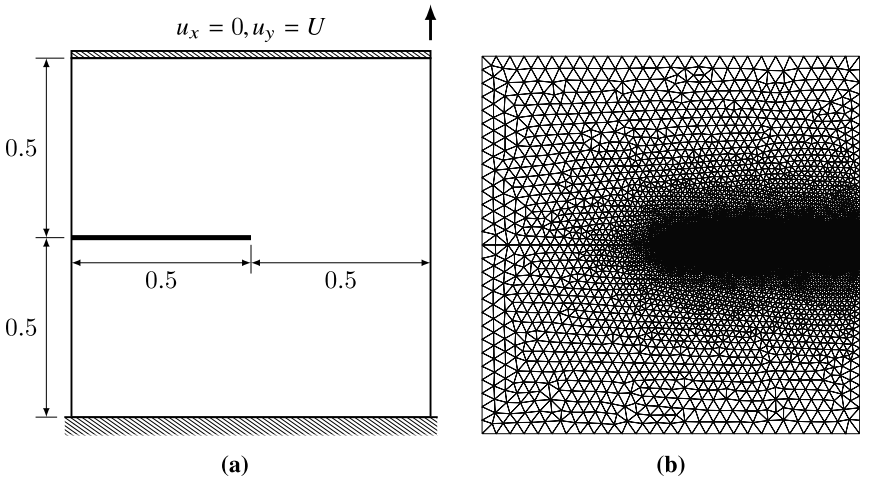

Fig. 7. Tension test of notched square specimen: (a) geometry and boundary conditions, (b) mesh refinement detail for $\ell/h = 2$.

Table 1
Details of individual simulations for the notched tension test.

ℓ/h	# Nodes	# Cells	# Unknowns, $\mathbf{u}$	# Unknowns, ϕ		Global matrix density, %		
				FE	FV	$\mathbf{u}$	ϕ, FE	ϕ, FV
1	3,542	6,889	6,972	–	6,889	0.1060	–	0.0361
2	6,567	12,906	13,022	6,567	12,906	0.0571	0.0604	0.0193
4	11,906	23,552	23,700	11,906	23,552	0.0315	0.0334	0.0106
6	17,031	33,784	33,950	17,031	33,784	0.0220	0.0234	0.0074
8	22,047	43,800	43,982	22,047	43,800	0.0170	0.0181	0.0057
10	27,832	55,360	55,552	27,832	55,360	0.0135	0.0143	0.0045
12	33,196	66,078	66,280	33,196	66,078	0.0113	0.0120	0.0038
16	43,297	86,266	86,482	43,297	–	0.0087	0.0092	–
20	53,776	107,212	107,440	53,776	–	0.0070	0.0074	–

where the dimensions are given in mm. Material parameters are set to the following: $E = 210,000$ MPa, $\nu = 0.3$, $\mathcal{G}_c = 2.7$ N/mm and $\ell = 0.0075$ mm. The loading consists of a uniform vertical displacement $U = 0.00575$ mm imposed at the upper boundary of the specimen and initially applied in increments of $\Delta u_y = 1.0 \times 10^{-4}$ mm until $u_y = 0.00525$, and then in smaller increments of $\Delta u_y = 1.0 \times 10^{-5}$ mm up to a final displacement of $u_y = U$. As the resulting stresses are predominantly tensile, we use the isotropic model given in (5) for the bulk response. Two sets of simulations are conducted, one pertaining to standard FE–FE interpolation and another for the proposed FE–FV scheme. In each set, the setup described above is solved repeatedly over several mesh realizations corresponding different ratios between the phase-field length scale ℓ and the characteristic size h of element edges at the refined region where the crack is expected to propagate. Note that for a given value of ℓ/h, the same generated mesh is used in conjunction with both formulations.

Table 1 lists the resulting number of unknowns as well as the density of the global coefficient matrices for the simulation runs conducted. As both schemes use P_1 finite elements to discretize the linear momentum equation, for a given mesh they share the same number of displacement unknowns. The FE–FV formulation has around twice the number of unknowns for the phase-field subsystem as the traditional scheme, however use of TPFA means that each row of the global coefficient matrix has at most four nonzero components. This is substantially less connectivity than the corresponding finite element scheme as reflected in the last two columns of Table 1, where the global matrix density has been calculated as

$$\text{Global matrix density, \%} = \frac{\text{\# nonzeros}}{(\text{\# unknowns})^2} \times 100. \tag{31}$$

As a consequence, the cost of assembling and solving the resulting linear equations is more or less the same for both FE–FE and FE–FV in 2D, as shown in Fig. 8(a). Moreover, use of FE–FV results in shorter simulation times for the current problem owing to the smaller number of iterations performed for a given ratio of ℓ/h, as can be seen from Figs. 8(b)–8(c).

The final phase-field profiles corresponding to $\ell/h = 2$ are shown in Fig. 9 along with the load–displacement curves for the two discretization schemes. For the range of ℓ/h ratios tested in the current example, we found the resulting load displacement curves to be virtually identical for the two methods, the only observable difference being the actual instances of failure. The latter are summarized in Fig. 10(a), where it can be seen that the critical load for the proposed FE–FV scheme has effectively converged with respect to mesh refinement at $\ell/h \approx 10$. In addition, the results show that the failure load predicted using a mesh refinement of $\ell/h = n$ in conjunction with the proposed scheme is roughly equivalent to one obtained by utilizing mesh with $\ell/h = 2n$ for FE–FE, which corroborates the findings from Section 4.1. We can thus infer that a critical load that is converged with respect to the mesh can be obtained with a mesh resolution of $\ell/h = 20$ in the crack path vicinity when using linear finite elements to discretize the phase-field. Incidentally, a mesh resolution of $\ell/h = 20$ was also used [53] to discretize the area around crack tips for a localized application of the phase-field model. On the other hand, it is well known that setting $\ell/h < 2$ results in a mesh that is too coarse for the FE–FE scheme, leading to a severe overestimation of failure loads. Remarkably, FE–FV yields a lower critical load for a relatively coarse discretization with $\ell/h = 1$ than FE–FE on a mesh with $\ell/h = 2$.

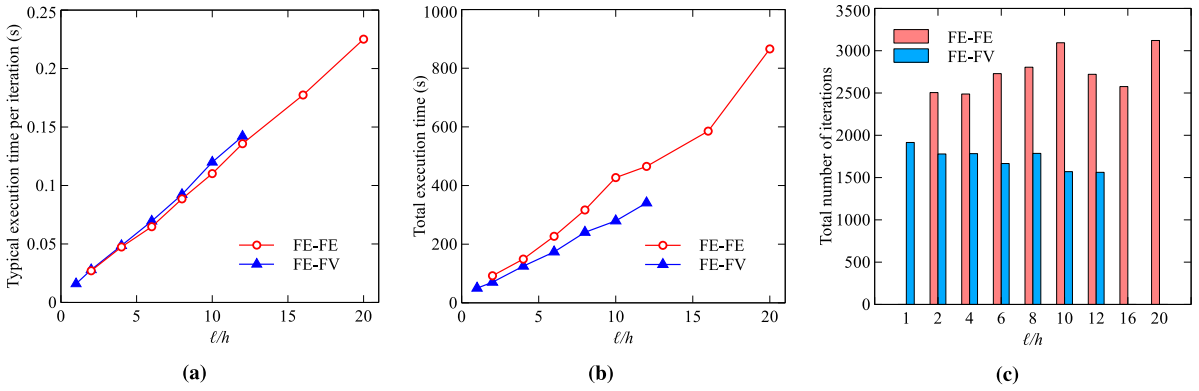

Fig. 8. Comparison of execution times for the notched tension test: (a) typical run times for a single iteration of the alternate minimization algorithm, (b) total simulation times inclusive of writing output, and (c) variation in total number of AM iterations with the choice of ℓ/h.

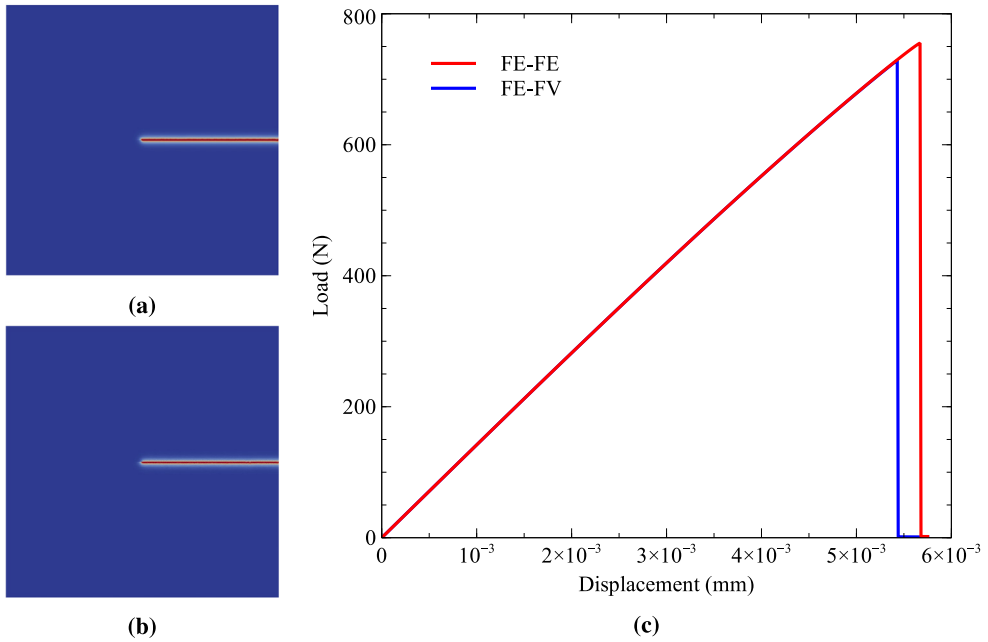

Fig. 9. Results for notched tension test with $\ell/h = 2$. Final crack path obtained using (a) standard FE–FE, and (b) the FE–FV scheme. (c) Load displacement curves for the two schemes.

An important point of comparison is the computational cost for obtaining a solution that is independent of the mesh for a given value of ℓ. This can be determined by plotting failure loads against the total execution time, as shown in Fig. 10(b). Assuming that the FE–FE formulation also converges to the same critical load ($P_{\text{cr}} = 714.26$ N) with mesh refinement, we can observe that the computational cost of attaining mesh-insensitive results for a given ℓ is reduced by almost 70% when using the proposed scheme over FE–FE. If a uniform discretization is to be used (for instance when the crack trajectory is unknown at the beginning of the simulation), then the cost difference between the two formulations will be even greater than what is currently observed. Note that we make no conclusions regarding actual accuracy of the critical loads with respect to the true solution, since this requires that the proper value of ℓ be used, or that the model must be modified to account for usage of a smaller or larger ℓ [25,51].

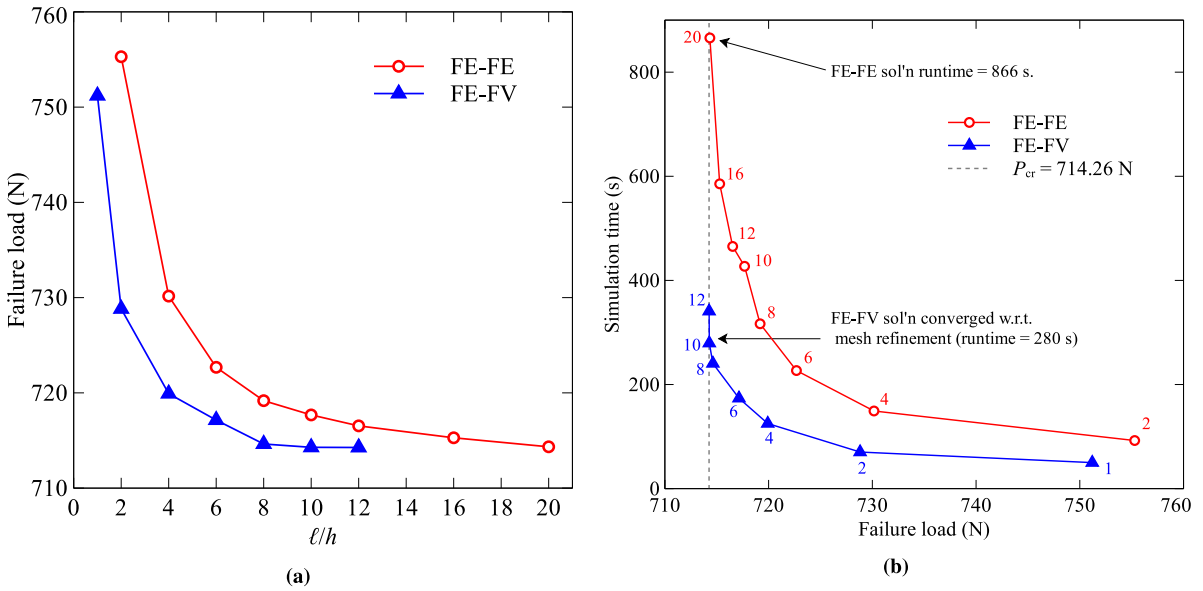

Fig. 10. Failure loads for the notched tension test, plotted against (a) different degrees of mesh refinement represented by ℓ/h, and (b) computational cost in terms of overall simulation time, where numbers beside data points indicate the ratio ℓ/h.

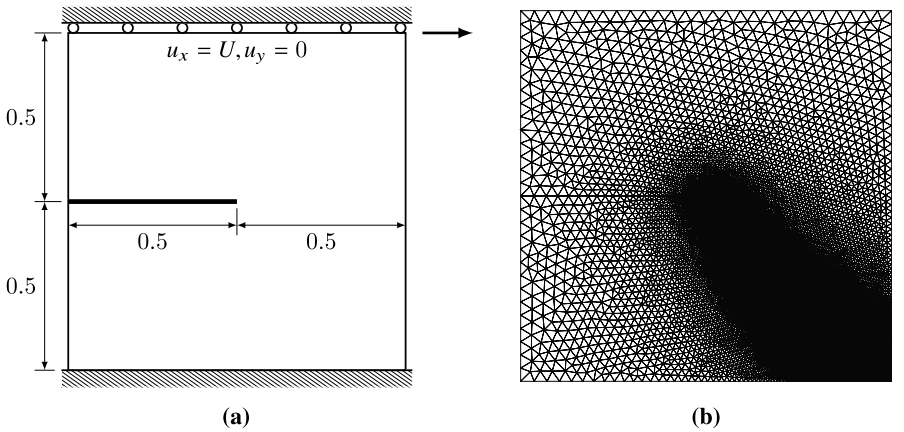

Fig. 11. Shear test of notched square specimen: (a) geometry and boundary conditions, and (b) mesh refinement detail for $\ell/h = 2$.

4.3. Shear loading of notched specimen

The same notched specimen from the previous problem is now subjected to shear loading by prescribing a constant horizontal displacement at its top boundary as depicted in Fig. 11. As in the previous example, meshes are refined a priori in the region where the crack is expected to propagate. The present benchmark problem derives from [45,49], however we note that there exists some variation across different studies on exactly what boundary conditions to apply. Our treatment here is similar to [59] in which the left and right sides of the specimen are kept traction free. Material parameters as well as the phase-field regularization parameter are the same as in the previous example, however for the current problem we make use of the anisotropic bulk degradation model of Amor et al. [56] in order to prevent the formation of cracks under compression. The imposed horizontal displacement at the top boundary is applied in increments of $\Delta u_x = 1 \times 10^{-4}$ mm until a cumulative value of $u_x = 0.0092$ mm, and thereafter the increments are decreased to $\Delta u_x = 1 \times 10^{-5}$ mm until the final displacement of $U = 0.013$ mm is reached. We make use of three different discretizations of the domain, representing varying levels of mesh

Table 2
Details of individual simulations for the notched shear test.

Run #	Method	ℓ/h	# Unknowns			Run time
			u	ϕ	Total	(h : min : s)
1	FE–FE	1	11,078	5,638	16,716	00 : 19 : 48
2	FE–FE	2	28,314	14,295	42,609	01 : 11 : 17
3	FE–FE	4	83,676	42,042	125,718	05 : 12 : 57
4	FE–FV	1	11,078	11,028	22,106	00 : 17 : 12
5	FE–FV	2	28,314	28,261	56,575	01 : 01 : 54
6	FE–FV	4	83,676	83,632	167,308	05 : 25 : 34

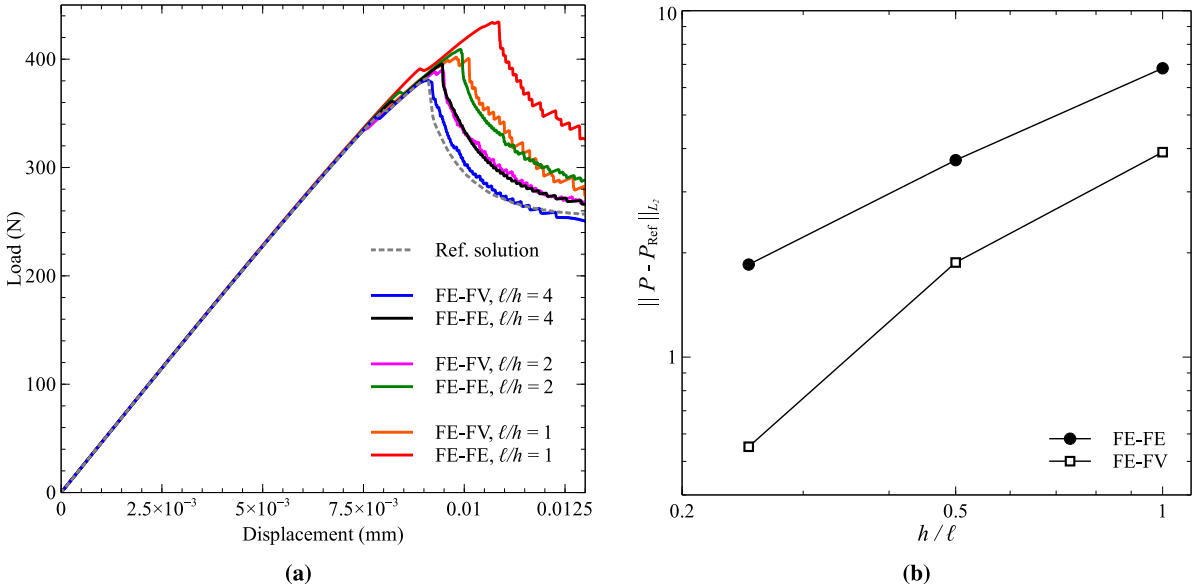

Fig. 12. Results for the notched shear test: (a) Load–displacement curves, and (b) error norms with respect to reference solution.

refinement ℓ/h in the region of crack propagation. A total of six simulation runs are conducted, with corresponding details reported in Table 2. Overall, we can observe that FE–FE and FE–FV yield comparable run times when applied to the same mesh.

Load–displacement curves obtained from the different simulations are plotted in Fig. 12(a) and exhibit the same qualitative behavior as reported in [59], with the difference in predicted peak loads attributable to the fact that we use a slightly larger value of ℓ in our simulations. Meanwhile, Fig. 12(b) shows the convergence behavior of FE–FE and FE–FV with regard to the load–displacement curve. Since an analytical solution is not available for the current problem, we have instead substituted a reference numerical solution obtained by using FE–FE in conjunction with mesh refined such that $\ell/h = 20$ in the region of fracture growth. The measure of error for the load–displacement curves can then be calculated as

$$\|P - P_{\text{Ref}}\|_{L_2} = \left(\int_0^U \left[P(u) - P_{\text{Ref}}(u) \right]^2 \, \mathrm{d}u \right)^{1/2}, \tag{32}$$

where u and P denote respectively the prescribed displacement and the total horizontal reaction force at the top boundary of the specimen. In terms of convergence with respect to mesh refinement, we note the similarity in relative behavior between the two methods for the current problem to the results shown in Fig. 6. In particular the post-peak behavior modeled by means of FE–FE in conjunction with a mesh characterized by $\ell/h = 4$ and FE–FV with $\ell/h = 2$ are nearly identical. The same observation can be made by comparing the simulated crack paths shown in Fig. 13. Here it is interesting to note the difference in crack trajectories obtained with the two methods

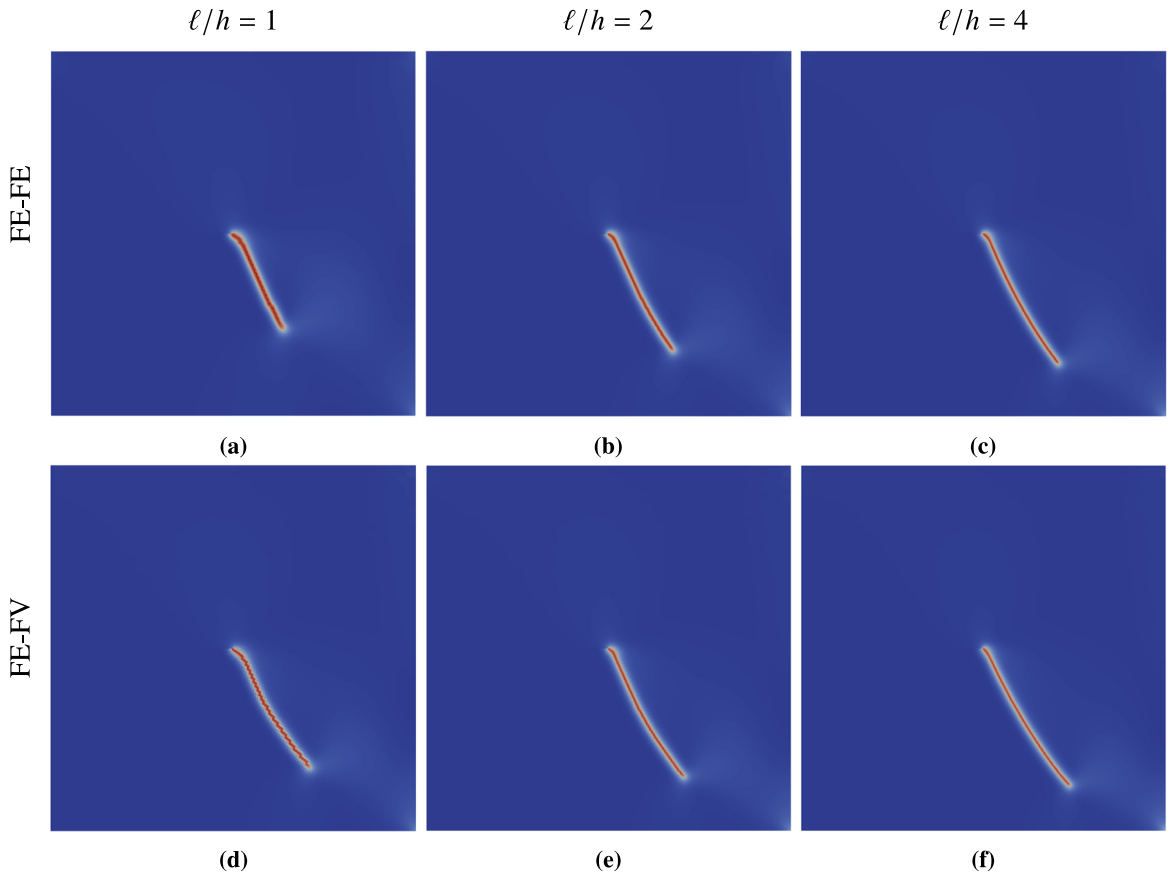

Fig. 13. Notched shear test: resulting crack paths for $u_x = 0.013$, obtained using FE–FE and FE–FV for different ratios of ℓ/h.

for $\ell/h = 1$. Despite the relative coarseness of the mesh with respect to ℓ, FE–FV is able to predict a curved crack path similar to simulations utilizing finer meshes. On the other hand, FE–FE produces a somewhat thicker crack with a considerably straighter trajectory, which appears upon closer scrutiny to be indicative of mesh dependence.[1] Given that the main value of such simulations lies in their predictive capability, the proper comparison to be made with regard to computational cost should then be between runs 2 and 4, and similarly between runs 3 and 5 in Table 2. From the reported run times, we can see that adoption of the FE–FV scheme in place of the traditional FE–FE formulation results in a reduction of around 75% in computational cost for the former case, and around 80% for the latter.

The evolution of bulk, surface and total energies with respect to the applied displacement are displayed in Fig. 14, where for clarity we show the results of runs 2 and 4 in one plot, along with runs 3 and 5 in a separate plot. Crack propagation in this particular example is stable for the entire magnitude of the prescribed displacement, which is applied in positive increments resulting in monotonically increasing total energy. We note that calculation of surface energy quantities is not straightforward with the proposed formulation, as the evaluation of integrals involving $\nabla\phi \cdot \nabla\phi$ is nontrivial for a cell-centered FV scheme. In the current work, this has been accomplished by performing a reconstruction of $\nabla\phi$ within each element as a post-processing step by utilizing the lowest order Raviart–Thomas (RT_0) basis functions together with the normal components of the phase-field gradient at element edges obtained using TPFA. Nevertheless, such reconstruction is not required for solving the discrete system of equations and hence does not influence the simulation results with regard to the calculated displacements and damage.

[1] In the simplex meshes generated with the frontal algorithm from [58], elements in the refined region are close to equilateral triangles whose arrangement is akin to a hexagonal structured grid. We observed that the crack path predicted by FE–FE for $\ell/h = 1$ is in fact orthogonal to a primary orientation of the said grid structure.

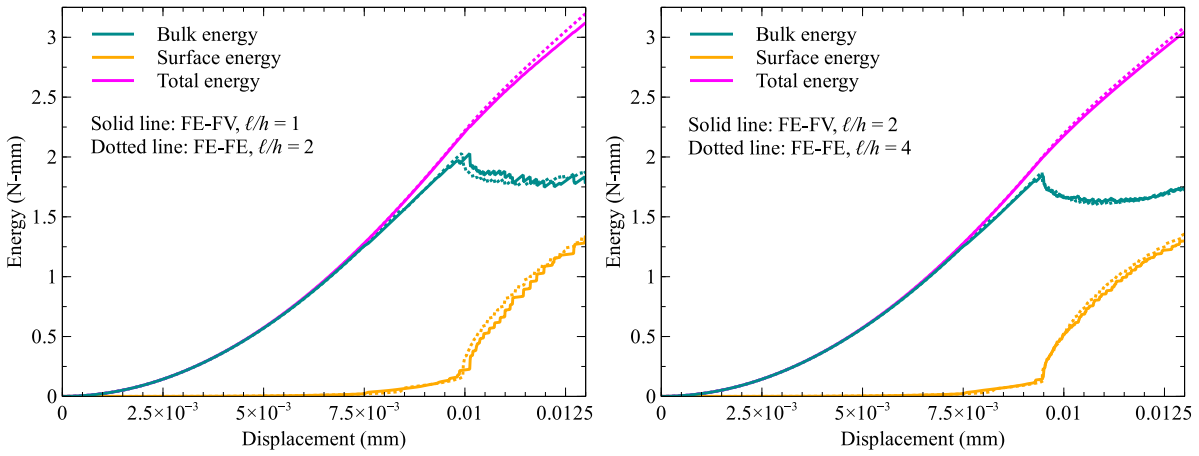

Fig. 14. Evolution of energy quantities for the notched shear test.

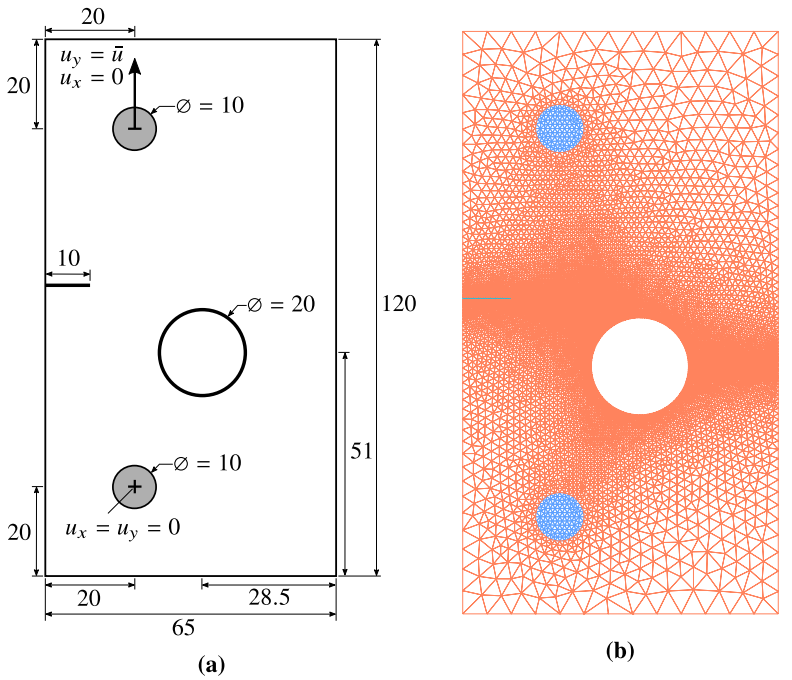

Fig. 15. Model setup for the problem of a notched plate with a hole, showing (a) geometry and boundary conditions, and (b) discretization of problem domain using simplex elements for $\ell/h = 2$. The simulated domain consists of the actual brittle specimen in which fracture occurs, and the upper and lower dowels (colored gray) that contain the points of load application. (For interpretation of the references to color in this figure legend, the reader is referred to the web version of this article.)

4.4. Stretching of notched plate with a hole

For the final example, we simulate crack propagation and subsequent nucleation in a notched specimen with an off-center hole based on the model setup given in [59]. The specimen geometry and boundary conditions along with a representative discretization are shown in Fig. 15. The prescribed displacements are applied as Dirichlet conditions at the center of the dowel portions of the specimen, which are modeled as linear elastic (non-damaging) with Young's modulus $E = 210$ GPa and Poisson ratio $\nu = 0.3$. The rest of the domain is treated as a linear elastic brittle material, for which the corresponding parameters are $E = 5.983$ GPa, $\nu = 0.22$, $\mathcal{G}_c = 2.28$ N/mm

Table 3
Details of individual simulations for the notched plate with a hole.

Run #	Method	ℓ/h	# Unknowns			Run time	P_{cr} (N)
			u	ϕ	Total	(h : min : s)	
1	FE–FE	1	7,542	3,579	11,121	0 : 04 : 37	495.62
2	FE–FE	2	15,400	7,488	22,888	0 : 09 : 34	475.97
3	FE–FE	4	35,106	17,301	52,407	0 : 21 : 03	464.25
4	FE–FE	8	88,008	43,672	131,680	0 : 55 : 21	460.22
5	FE–FV	1	7,542	6,929	14,471	0 : 05 : 08	478.40
6	FE–FV	2	15,400	14,671	30,071	0 : 09 : 23	464.21
7	FE–FV	4	35,106	34,171	69,277	0 : 22 : 30	461.09
8	FE–FV	8	88,008	86,687	174,695	1 : 01 : 45	458.96

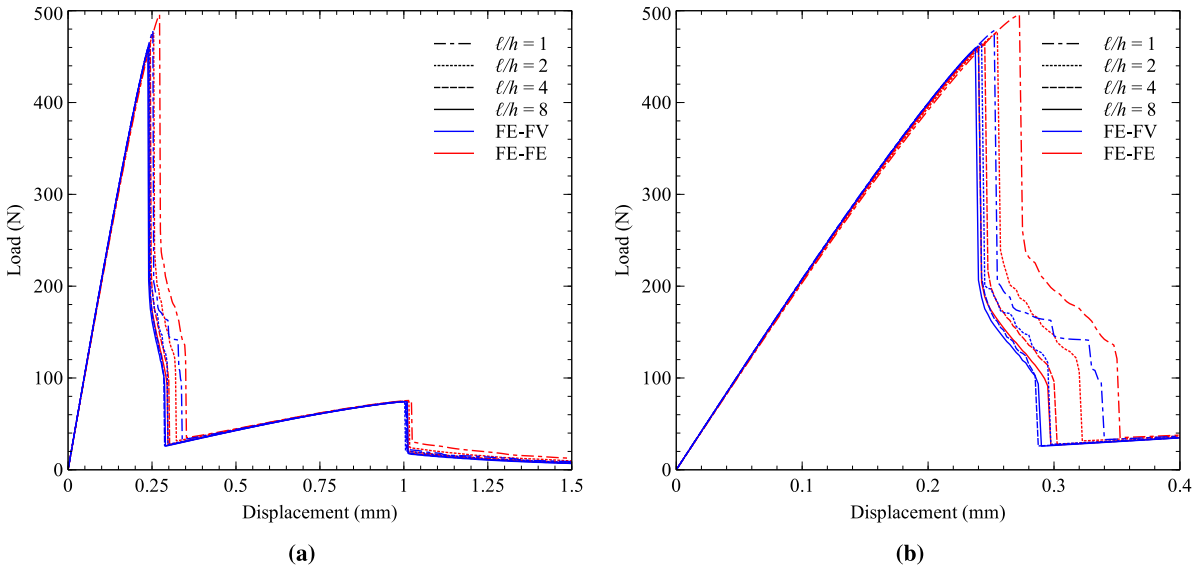

Fig. 16. Load–displacement curves for the notched plate with a hole. The full set of curves obtained in the simulations are shown in (a); for clarity, the portion of load–displacement response corresponding to the brutal–stable–brutal propagation of the initial crack until it intersects the hole is shown in (b).

and $\ell = 1.0$ mm. The notch is modeled by initializing the phase-field profile using Dirichlet-type constraints as discussed in Section 3.3. The prescribed upward displacement at the upper dowel is applied in increments of 0.0025 mm until a final displacement of $\bar{u} = 1.5$ mm is reached.

Details of the discretization along with run times and obtained critical loads for the initial crack propagation are listed in Table 3. It can be observed for instance that runs 3 and 6 yield essentially the same value of the critical load, but with the computational cost of the latter being roughly 45% of the former. Similarly, runs 4 and 7 predict critical loads in near vicinity of the other, where the cost of running the FE–FV simulation is around 41% of its FE–FE counterpart.

Fig. 16 shows the resulting load–displacement curves obtained with both FE–FE and FE–FV formulations for different ℓ/h ratios, in which plotted load values correspond to the resultant force induced at the center of the upper dowel where upward displacement is imposed. For all simulations performed, fracture is observed to take place as follows: first the notch extends horizontally in a brutal manner, and then propagates in stable fashion along a curved path towards the hole before undergoing another brutal phase at which the crack finally intersects the hole boundary. Thereafter the specimen behavior can be characterized as essentially linear elastic, up to a point where a second horizontal crack nucleates from the hole. Initial crack growth accompanying said nucleation is brutal, with subsequent propagation occurring in a stable manner. These different stages are shown in Fig. 17 for the two

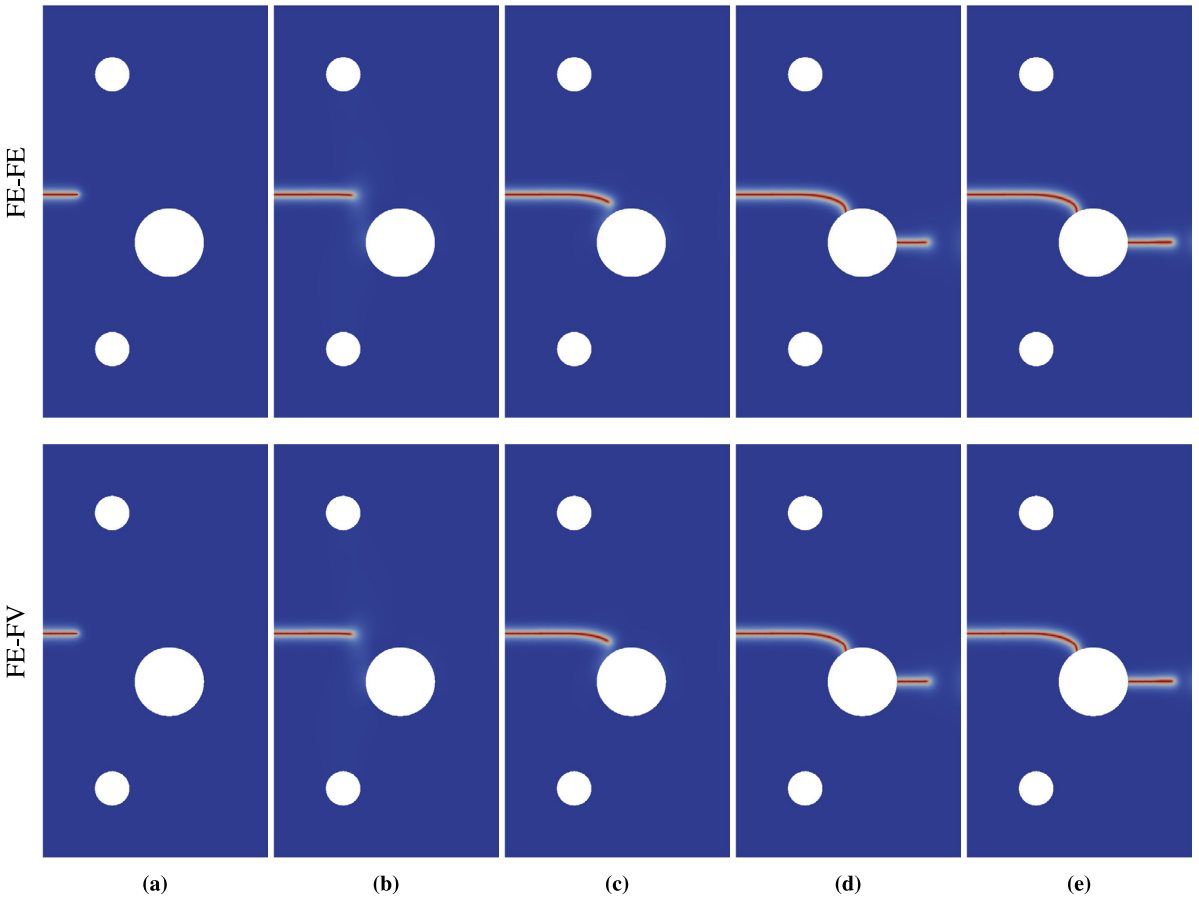

Fig. 17. Crack propagation in notched plate with a hole: (a) initial phase-field profile, (b) immediately after first brutal crack growth, (c) at end of stable propagation phase, (d) immediately after nucleation of second crack from hole boundary, (e) at end of simulation.

formulations studied in this work. Note that we have included results corresponding to $\ell/h = 1$ mainly for purposes of comparison; it is well known that for linear finite elements one should choose h to be smaller than ℓ.

Evolution of energy quantities over the course of simulation are given in Fig. 18. We can observe that both FE–FE and FE–FV yield total energy curves that are not monotonically increasing. This contradicts what is expected in this case since the imposed displacement $\bar{u}$ is strictly increasing from 0 over time and the resulting reaction forces are always positive as evident from Fig. 16. On the other hand, the effective applied external work as a function of the imposed displacement can be obtained easily by integration of the load–displacement curve and addition of the surface energy associated with preexisting cracks modeled via the phase-field. Fig. 19 shows the evolution of the external work together with the total energy using data from the FE–FE results for $\ell/h = 8$. We can see that the two curves initially coincide, however deviations are introduced for each instance of brutal cracking. These correspond to energy loss, and their occurrence in conjunction with brutal cracking can be interpreted as a transformation of the missing component into kinetic energy (at which point the quasi-static assumptions of the adopted phase-field model no longer apply). However if the brutal crack propagation does not completely cut the specimen into unconnected parts and the latter remains sufficiently constrained, then it should be possible to reach a static configuration that satisfies energy conservation and wherein the aforementioned kinetic component has been converted back to potential energy. In such a case, the implication is that the solution obtained during a brutal cracking step using standard quasi-static assumptions underestimates the length of crack advance since the source term in the phase-field equation is missing this converted kinetic component.

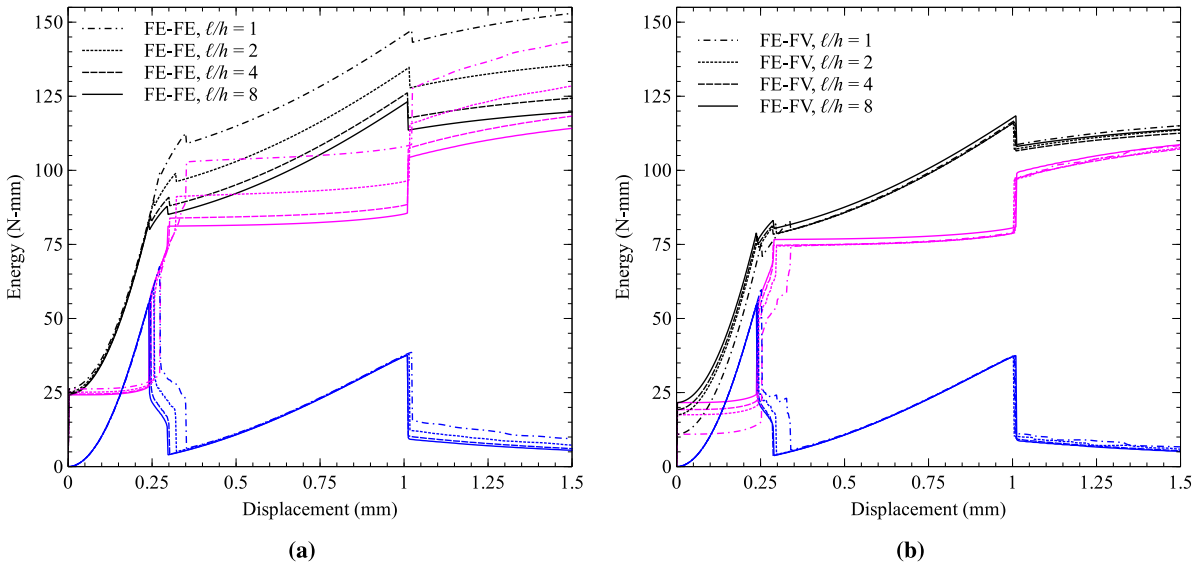

Fig. 18. Evolution of energy quantities for the notched plate with a hole subjected to tensile loading, showing results obtained using (a) FE–FE, and (b) FE–FV. The blue, magenta and black curves correspond respectively to bulk, surface and total (surface + bulk) energies. (For interpretation of the references to color in this figure legend, the reader is referred to the web version of this article.)

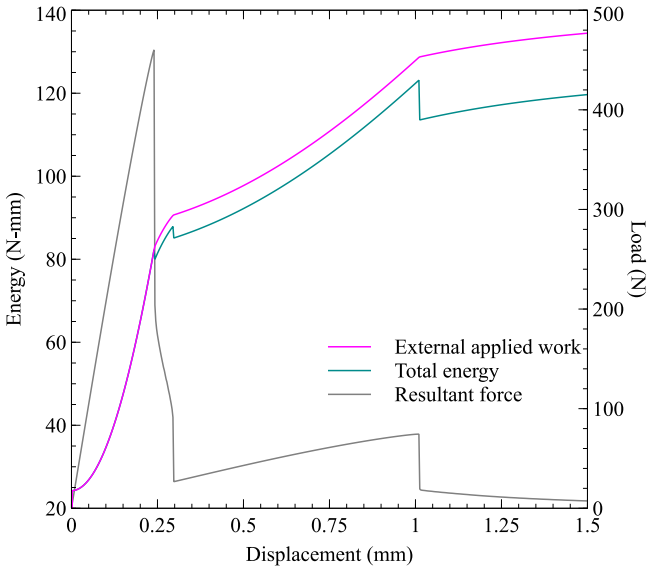

Fig. 19. Simulation results for FE–FE, $\ell/h = 8$: resultant load, external applied work and total energy.

5. Concluding remarks

In this paper we have introduced an unequal-order discretization scheme for brittle fracture phase-field models that combines P_1 finite element and cell-centered (P_0) finite volume approaches. This was motivated by the inference that mesh size restrictions with respect to the phase-field length scale may be much more stringent than the requirements to obtain sufficiently accurate solution of the stresses, due to the fact that introduction of damage at the crack tips eliminates stress singularities. Application of the proposed formulation to several popular benchmark problems in the literature have shown that the computational cost of obtaining mesh-insensitive results

are significantly reduced in comparison with an equal-order (P_1) finite element discretization of the mechanics and phase-field equations. This is rather counter-intuitive looking at the degrees of polynomial approximation, but may be explained by the fact that the manner in which flux/gradients are calculated across cell faces in the FV framework allows for the implicit occurrence of a cusp inside the control volume and can thus capture the lack of regularity in the phase-field profile more efficiently. As most implementations of fracture phase-field models in the literature utilize equal-order formulations, we consider this work as a proof of concept regarding the potential of using unequal-order and combined discretization approaches to overcome particular challenges associated with the 2nd order phase-field formulation.

Declaration of competing interest

The authors declare that they have no known competing financial interests or personal relationships that could have appeared to influence the work reported in this paper.

Acknowledgments

This work was funded by the Research Council of Norway through Grant No. 228832/E20 and Equinor ASA through the Akademia agreement.

Appendix. Implementation of strain decomposition for anisotropic bulk degradation

In the code utilized for the current work, the isotropic and anisotropic formulations given in (5) and (6) are implemented as different constitutive models in conjunction with a single numerical framework that corresponds to the discretized field equations. These in turn utilize predefined modulus tensors for linear elasticity corresponding to plane strain, written in Voigt form as

$$\mathbb{C}^e = \begin{bmatrix} \lambda + 2\mu & \lambda & \lambda & 0 \\ \lambda & \lambda + 2\mu & \lambda & 0 \\ \lambda & \lambda & \lambda + 2\mu & 0 \\ 0 & 0 & 0 & \mu \end{bmatrix}, \tag{A.1}$$

where λ and μ are the Lamé coefficients. As shown above, the matrix dimensions of $\mathbb{C}^e$ are 4×4 since for applications involving plasticity, the z-component of plastic strain may be nonzero even if $\varepsilon_{zz} = 0$. On the other hand in the bulk degradation model of Amor et al. [56], the strain tensor is split into volumetric/spherical and deviatoric components, with the former used as a reference quantity for modeling mode I fracture and unilateral contact, and the latter for cracking in mode II. Thus in plane strain problems, one can argue that the deviatoric component of strain in the z-direction should not play a role in mode I/II fracture evolution as it instead implies cracking in mode III. Consequently, we perform the strain decomposition considering only two dimensions. Writing the strain in Voigt form as $\boldsymbol{\varepsilon} = \left\{\varepsilon_{xx}, \varepsilon_{yy}, 0, \gamma_{xy}\right\}^{\mathrm{T}}$, we calculate volumetric and deviatoric components as

$$\begin{aligned} \boldsymbol{\varepsilon}_{\mathrm{vol}} &= \mathbb{P}\boldsymbol{\varepsilon} \\ \boldsymbol{\varepsilon}_{\mathrm{dev}} &= (\mathbb{I} - \mathbb{P})\,\boldsymbol{\varepsilon} \end{aligned} \tag{A.2}$$

where

$$\mathbb{P} = \frac{1}{2}\begin{bmatrix} 1 & 1 & 0 & 0 \\ 1 & 1 & 0 & 0 \\ 0 & 0 & 0 & 0 \\ 0 & 0 & 0 & 0 \end{bmatrix} \text{ and } \mathbb{I} = \begin{bmatrix} 1 & 0 & 0 & 0 \\ 0 & 1 & 0 & 0 \\ 0 & 0 & 1 & 0 \\ 0 & 0 & 0 & 1 \end{bmatrix}. \tag{A.3}$$

The above formula yields $\varepsilon_{\mathrm{vol},zz} = \varepsilon_{\mathrm{dev},zz} = 0$, hence $\boldsymbol{\varepsilon}_{\mathrm{vol}}$ is no longer a spherical tensor. Denoting by $H(\bullet)$ the Heaviside step function, the tangent modulus accounting for damage is given by

$$\mathbb{C}(\boldsymbol{\varepsilon}, \phi) = g(\phi)\,\mathbb{C}^e\left\{[H(\operatorname{tr}\boldsymbol{\varepsilon}) - 1]\,\mathbb{P} + \mathbb{I}\right\} + H(-\operatorname{tr}\boldsymbol{\varepsilon})\,\mathbb{C}^e\mathbb{P} \tag{A.4}$$

which will not be symmetric due to the form of $\mathbb{P}$. Nevertheless, the product $\mathbf{B}^{\mathrm{T}}\mathbb{C}(\boldsymbol{\varepsilon}, \phi)\,\mathbf{B}$ yields a symmetric matrix as the third row of $\mathbf{B}$ is composed entirely of zeros.

References

[1] A. Griffith, The phenomena of rupture and flow in solids, Philos. T. R. Soc. A 221 (1921) 163–198.
[2] C.E. Inglis, Stresses in plates due to the presence of cracks and sharp corners, Trans. INA 55 (1913) 219–241.
[3] G. Irwin, Analysis of stresses and strains near the end of a crack traversing a plate, J. Appl. Mech. 24 (1957) 361–364.
[4] G.A. Francfort, J.-J. Marigo, Revisiting brittle fracture as an energy minimization problem, J. Mech. Phys. Solids 46 (8) (1998) 1319–1342.
[5] D. Ngo, A.C. Scordelis, Finite element analysis of reinforced concrete beams, J. Am. Concr. Instrum. 64 (1967) 152–163.
[6] Y.R. Rashid, Ultimate strength analysis of prestressed concrete pressure vessels, Nucl. Eng. Des. 7 (1968) 334–344.
[7] X.-P. Xu, A. Needleman, Numerical simulations of fast crack growth in brittle solids, J. Mech. Phys. Solids 42 (9) (1994) 1397–1434.
[8] G.T. Camacho, M. Ortiz, Computational modelling of impact damage in brittle materials, Int. J. Solids Struct. 33 (1996) 2899–2938.
[9] R.S. Barsoum, Triangular quarter-point elements as elastic and perfectly-plastic crack tip elements, Int. J. Numer. Meth. Engng. 11 (1977) 85–98.
[10] T. Belytschko, T. Black, Elastic crack growth in finite elements with minimal remeshing, Int. J. Numer. Meth. Engng. 45 (1999) 601–620.
[11] N. Moës, J. Dolbow, T. Belytschko, A finite element method for crack growth without remeshing, Int. J. Numer. Meth. Engng. 46 (1999) 131–150.
[12] A. Hillerborg, M. Modéer, P.-E. Petersson, Analysis of crack formation and crack growth in concrete by means of fracture mechanics and finite elements, Cem. Concr. Res. 6 (6) (1976) 773–781.
[13] A.K. Gupta, H. Akbar, Cracking in reinforced concrete analysis, J. Struct. Eng. 110 (1984) 1735–1746.
[14] Z.P. Bazant, B. Oh, Crack band theory for fracture of concrete, Mater. Struct. 16 (3) (1983) 155–177.
[15] G. Pijaudier-Cabot, Z. Bazant, Nonlocal damage theory, J. Eng. Mech. 113 (1987) 1512–1533.
[16] R.H.J. Peerlings, R. de Borst, W.A.M. Brekelmans, J.H.P. De Vree, Gradient enhanced damage for quasi-brittle materials, Int. J. Numer. Meth. Engng. 39 (1996) 3391–3403.
[17] R.H.J. Peerlings, R. de Borst, W.A.M. Brekelmans, M.G.D. Geers, Gradient-enhanced damage modelling of concrete fracture, Mech. Cohes.-Frict. Mater. 3 (1998) 323–342.
[18] B. Bourdin, G.A. Francfort, J.-J. Marigo, Numerical experiments in revisited brittle fracture, J. Mech. Phys. Solids 48 (2000) 797–826.
[19] B. Bourdin, G.A. Francfort, J.-J. Marigo, The variational approach to fracture, J. Elasticity 91 (2008) 5–148.
[20] C. Kuhn, R. Müller, A continuum phase field model for fracture, Eng. Fract. Mech. 77 (2010) 3625–3634.
[21] A. Braides, Approximation of Free-Discontinuity Problems, in: Lecture Notes in Mathematics, vol. 1694, Springer Berlin Heidelberg, 2006.
[22] K. Pham, H. Amor, J.-J. Marigo, C. Maurini, Gradient damage models and their use to approximate brittle fracture, Int. J. Damage Mech. 20 (2011) 618–652.
[23] P. Sicsic, J.-J. Marigo, From gradient damage laws to Griffith's theory of crack propagation, J. Elasticity 113 (2013) 55–74.
[24] B. Bourdin, J.-J. Marigo, C. Maurini, P. Sicsic, Morphogenesis and propagation of complex cracks induced by thermal shocks, Phys. Rev. Lett. 112 (2014) 014301.
[25] E. Tanné, T. Li, B. Bourdin, J.-J. Marigo, C. Maurini, Crack nucleation in variational phase-field models of brittle fracture, J. Mech. Phys. Solids 110 (2018) 80–99.
[26] B. Bourdin, C. Maurini, M. Knepley, Secondary thermal cracks in EGS: A variational approach, GRC Trans. 34 (2010) 319–322.
[27] A. Abdollahi, I. Arias, Phase-field modeling of the coupled microstructure and fracture evolution in ferroelectric single crystals, Acta Mater. 59 (2011) 4733–4746.
[28] Z.A. Wilson, M.J. Borden, C.M. Landis, A phase-field model for fracture in piezoelectric ceramics, Int. J. Fract. 183 (2013) 135–153.
[29] A. Mikelić, M.F. Wheeler, T. Wick, A quasi-static phase-field approach to pressurized fractures, Nonlinearity 28 (2015) 1371–1399.
[30] A. Mikelić, M.F. Wheeler, T. Wick, Phase-field modeling of a fluid-driven fracture in a poroelastic medium, Comput. Geosci. 19 (2015) 1171–1195.
[31] C. Miehe, S. Mauthe, S. Teichtmeister, Minimization principles for the coupled problem of Darcy-Biot-type fluid transport in porous media linked to phase field modeling of fracture, J. Mech. Phys. Solids 82 (2015) 186–217.
[32] C. Miehe, S. Mauthe, Phase field modeling of fracture in multi-physics problems. Part III. Crack driving forces in hydro-poro-elasticity and hydraulic fracturing of fluid-saturated porous media, Comput. Methods Appl. Mech. Engrg. 304 (2016) 609–655.
[33] K. Yoshioka, B. Bourdin, A variational hydraulic fracturing model coupled to a reservoir simulator, Int. J. Rock Mech. Min. Sci. 88 (2016) 137–150.
[34] T. Cajuhi, L. Sanavia, L. De Lorenzis, Phase-field modeling of fracture in variably saturated porous media, Comput. Mech. 61 (3) (2018) 229–318.
[35] M. Klinsmann, D. Rosato, M. Kamlah, R.M. McMeeking, Modeling crack growth during Li insertion in storage particles using a fracture phase field approach, J. Mech. Phys. Solids 92 (2016) 313–344.
[36] C. Miehe, H. Dal, L.-M. Schänzel, A. Raina, A phase-field model for chemo-mechanical induced fracture in lithium-ion battery electrode particles, Int. J. Numer. Meth. Engng. 106 (2016) 683–711.
[37] S. Burke, C. Ortner, E. Süli, An adaptive finite element approximation of a variational model of brittle fracture, SIAM J. Numer. Anal. 48 (3) (2010) 980–1012.
[38] M.J. Borden, C.V. Verhoosel, M.A. Scott, T.J.R. Hughes, C.M. Landis, A phase-field description of dynamic brittle fracture, Comput. Methods Appl. Mech. Engrg. 217–220 (2012) 77–95.
[39] S. Burke, C. Ortner, E. Süli, An adaptive finite element approximation of a generalized Ambrosio–Tortorelli functional, Math. Models Methods Appl. Sci. 23 (9) (2013) 1663–1697.

[40] T. Heister, M.F. Wheeler, T. Wick, A primal-dual active set method and predictor-corrector mesh adaptivity for computing fracture propagation using a phase-field approach, Comput. Methods Appl. Mech. Engrg. 290 (2015) 466–495.
[41] M. Klinsmann, D. Rosato, M. Kamlah, R.M. McMeeking, An assessment of the phase field formulation for crack growth, Comput. Methods Appl. Mech. Engrg. 294 (2015) 313–330.
[42] T. Wick, Goal functional evaluations for phase-field fracture using PU-based DWR mesh adaptivity, Comput. Mech. 57 (2016) 1017–1035.
[43] M. Artina, M. Fornasier, S. Micheletti, S. Perotto, Anisotropic mesh adaptation for crack detection in brittle materials, SIAM J. Sci. Comput. 37 (4) (2015) B633–B659.
[44] M.J. Borden, T.J.R. Hughes, C.M. Landis, C.V. Verhoosel, A higher-order phase-field model for brittle fracture: Formulation and analysis within the isogeometric analysis framework, Comput. Methods Appl. Mech. Engrg. 273 (2014) 100–118.
[45] C. Miehe, M. Hofacker, F. Welschinger, A phase field model for rate-independent crack propagation: Robust algorithmic implementation based on operator splits, Comput. Meth. Appl. Mech. Engrg. 199 (2010) 2765–2778.
[46] J. Vignollet, S. May, R. de Borst, C.V. Verhoosel, Phase-field models for brittle and cohesive fracture, Meccanica 49 (2014) 2587–2601.
[47] T. Gerasimov, L. De Lorenzis, A line search assisted monolithic approach for phase-field computing of brittle fracture, Comput. Methods Appl. Mech. Engrg. 312 (2016) 276–303.
[48] P. Farrell, C. Maurini, Linear and nonlinear solvers for variational phase-field models of brittle fracture, Int. J. Numer. Meth. Engng. 109 (2017) 648–667.
[49] C. Miehe, F. Welschinger, M. Hofacker, Thermodynamically consistent phase-field models of fracture: variational principles and multi-field FE implementations, Int. J. Numer. Meth. Engng. 83 (10) (2010) 1273–1311.
[50] T.T. Nguyen, J. Yvonnet, Q.-Z. Zhu, M. Bornert, C. Chateau, A phase field method to simulate crack nucleation and propagation in strongly heterogeneous materials from direct imaging of their microstructure, Eng. Fract. Mech. 139 (2015) 18–39.
[51] J.M. Sargado, E. Keilegavlen, I. Berre, J.M. Nordbotten, High-accuracy phase-field models for brittle fracture based on a new family of degradation functions, J. Mech. Phys. Solids 111 (2018) 458–489.
[52] B. Li, C. Peco, D. Millán, I. Arias, M. Arroyo, Phase-field modeling and simulation of fracture in brittle materials with strongly anisotropic surface energy, Int. J. Numer. Meth. Engng. 102 (2015) 711–727.
[53] B. Giovanardi, A. Scotti, L. Formaggia, A hybrid XFEM-Phase field (Xfield) method for crack propagation in brittle elastic materials, Comput. Methods Appl. Mech. Engrg. 320 (2017) 396–420.
[54] D. Santillán, R. Juanes, L. Cueto-Felgueroso, Phase field model of fluid-driven fracture in elastic media: Immersed-fracture formulation and validation with analytical solutions, J. Geophys. Res. Solid Earth 122 (2017) 2565–2589.
[55] I. Aavatsmark, T. Barkve, Ø. Bøe, T. Mannseth, Discretization on non-orthogonal, quadrilateral grids for inhomogeneous, anisotropic media, J. Comput. Phys. 127 (1996) 2–14.
[56] Hanen Amor, Jean-Jacques Marigo, Corrado Maurini, Regularized formulation of the variational brittle fracture with unilateral contact: Numerical experiments, J. Mech. Phys. Solids 57 (2009) 1209–1229.
[57] J.M. Sargado, A new object-oriented framework for solving multiphysics problems via combination of different numerical methods, 2019, arXiv:1905.00104 [cs.MS].
[58] C. Geuzaine, J.-F. Remacle, Gmsh: A 3-D finite element mesh generator with built-in pre- and post-processing facilities, Int. J. Numer. Meth. Engng. 79 (2009) 1309–1331.
[59] M. Ambati, T. Gerasimov, L. De Lorenzis, A review on phase-field models of brittle fracture and a new fast hybrid formulation, Comput. Mech. 55 (2015) 383–405.